



Title	Pavement design method in Japan with consideration of climate effect and principal stress axis rotation
Author(s)	Lin, Tianshu; Ishikawa, Tatsuya; Maruyama, Kimio; Tokoro, Tetsuya
Citation	Transportation geotechnics, 28, 100552 https://doi.org/10.1016/j.trgeo.2021.100552
Issue Date	2021-05
Doc URL	http://hdl.handle.net/2115/88577
Rights	© <2021>. This manuscript version is made available under the CC-BY-NC-ND 4.0 license http://creativecommons.org/licenses/by-nc-nd/4.0/
Rights(URL)	http://creativecommons.org/licenses/by-nc-nd/4.0/
Type	article (author version)
File Information	Manuscript-Lin Tianshu-revised.pdf



[Instructions for use](#)

1 Pavement design method in Japan with consideration of climate effect and principal stress axis
2 rotation

3

4 Tianshu Lin ^a, Tatsuya Ishikawa ^{b*}, Kimio Maruyama ^c, Tetsuya Tokoro ^d

5 ^a Graduate School of Engineering, Hokkaido University, Kita 13, Nishi 8, Kita-Ku, Sapporo
6 060-8628, Japan

7 ^b Faculty of Engineering, Hokkaido University, Kita 13, Nishi 8, Kita-Ku, Sapporo 060-8628,
8 Japan

9 ^c Cold-Region Maintenance Engineering Research Group, Civil Engineering Research Institute
10 for Cold Region, 1-34, Hiragishi 1, 3, Toyohira-ku, Sapporo 062-8602, Japan

11 ^d Faculty of Engineering, Hokkai-Gakuen University, 1-1, Minami 26 Nishi 11, Chuo-ku, Sap-
12 poro 064-0926, Japan

13 **Key words**

14 Rutting; Fatigue cracking; Freeze-thaw action; Resilient modulus; Mechanical-empirical de-
15 sign method

16 **Abstract**

17 Current Japanese design guide uses mechanical-empirical criteria to predict the failure loading
18 number against fatigue cracking and rutting. However, these criteria have some limitations that

* Corresponding author. Email address: t-ishika@eng.hokudai.ac.jp

19 the variation in moduli of base and subgrade layer due to the fluctuation in water contents,
20 freeze-thaw history, and stress states are not considered. As well known, these factors greatly
21 affect the soil mechanical properties like resilient modulus. Besides, present rutting failure cri-
22 terion provides no indication of the behavior of rutting over time, and the effect of principal stress
23 axis rotation on rutting development is also not captured. To overcome such limitations, this study
24 modified the present Japanese pavement design method through the following two main aspects:
25 (1) Replacing constant elastic modulus of base and subgrade layer to resilient modulus related
26 to stress states and complex climate conditions, which are defined as the combination of fluc-
27 tuating water content and freeze-thaw action; (2) Modifying rutting failure criterion by consid-
28 ering generally used MEPDG model and also the effect of principal stress axis rotation. All
29 modifications are performed based on laboratory element test like suction-controlled freeze-
30 thaw triaxial test, which could simulate complex climate conditions, and multi-ring shear test,
31 which could simulate principal stress axis rotation. Besides, modified criteria are examined by
32 comparing to long-term measured performance of test pavements built in Hokkaido, the north
33 island of Japan. Modified Japanese pavement design method shows high applicability and ac-
34 curacy on the pavement life prediction, especially for the flexible pavement in cold regions like
35 Hokkaido.

36 **1. Introduction**

37 Mechanistic-Empirical Pavement Design Guide (MEPDG), which combines empirical and
38 mechanistic concepts, uses input data such as materials, traffic, climate, and for a trial design
39 calculates mechanistically stresses and strains, which are subsequently used in empirical

40 distress models to compute damage accumulated over time like rutting, fatigue cracking, and
41 thermal cracking. MEPDG has been mainly used in the United States. At the current time with
42 regard to Japan, a mechanistic-empirical method based only on a multi-layer linear elastic
43 model is still currently being used and as a consequence, the applicability and prediction preci-
44 sion are unsatisfactory.

45 To be precise, several serious drawbacks limit the applicability and accuracy of present Japa-
46 nese pavement design method. First, constant base and subgrade layer moduli through the
47 whole year based on linear elastic theory restrict the precision since soil shows nonlinear elastic
48 property in small strain period as reviewed by Clayton [2011]. Based on such nonlinearity,
49 resilient modulus (M_r) is proposed [Seed, 1955] to capture the effect of stress states on the
50 stiffness of soil. M_r is widely used in Mechanistic-Empirical Pavement Design Guide (MEPDG)
51 and estimated by Eq. (1), named as the universal model [AASHTO, 2008]. According to Eq.
52 (1), the resilient modulus decreases with increasing deviator stress and decreasing confining
53 pressure. In general, based on laboratory element test results, resilient modulus of base course
54 and subgrade material are determined and employed as the layer moduli in a multi-layered
55 elastic pavement response model.

$$56 \quad M_r = k_1 p_a \left(\frac{\theta}{p_a} \right)^{k_2} \left(\frac{\tau_{oct}}{p_a} + 1 \right)^{k_3} \quad (1)$$

57 where k_1 , k_2 , k_3 are regression constants; p_a is atmospheric pressure and set as 101 kPa in this
58 study; θ is bulk stress (kPa); τ_{oct} is octahedral stress (kPa).

59 Second, effects of water content and freeze-thaw action, which greatly influence the stiffness of
60 base and subgrade layer [Berg et al., 1996; Cole et al., 1981; Johnson et al., 1978; Simonsen et
61 al., 2002; Simonsen and Isacsson, 2001], are not considered in Japanese pavement design method.

62 To be precise, rising water content, as a result of the inflow of water during rainfall or the
 63 thawing of ice lenses, causes a temporary decrease in the stiffness of base course and subgrade
 64 materials. Meanwhile, freeze-thaw action always decreases moduli of base and subbase layer
 65 materials even with no excess water storage after thawing [Ishikawa et al., 2019a; Lin et al.,
 66 2019b], as ice formation tends to break some of the particle contacts and interlocking of soil
 67 particles and finally deteriorates the soil structure uniformity and stiffness.

68 Third, current rutting model cannot capture the behavior of rutting over time or with the applica-
 69 tion of traffic loading. It also does not consider rate-hardening or the contribution of the non-
 70 subgrade layers to rutting. To overcome these limitations, MEPDG proposed a rutting depth pre-
 71 diction model [NCHRP, 2004], which converts the plastic strain measured from the laboratory
 72 to the field condition, as shown in Eq. (2).

$$73 \quad \varepsilon_p(N) = \beta_1 k_1 \left(\frac{\varepsilon_0}{\varepsilon_r}\right) e^{-\left(\frac{\rho}{N}\right)^\beta} \varepsilon_v \quad (2)$$

74 where $\varepsilon_p(N)$ is permanent strain for the layer/sub-layer; N is number of traffic repetitions; ε_0 , β ,
 75 and ρ are material properties; ε_r is resilient strain imposed in laboratory test to obtain material
 76 properties ε_0 , β , and ρ ; ε_v is average vertical resilient strain in the layer, which is calculated by
 77 a multi-layer elastic pavement response model; β_1 is calibration factor for the unbound granular
 78 and subgrade materials; k_1 is global calibration coefficients.

79 Last, the rutting failure criterion in Japanese pavement design guide as well as MEPDG rutting
 80 model does not capture the effect of principal stress axis rotation (PSAR), which is a phenom-
 81 enon caused by moving wheel loads and greatly amplifies the permanent deformation of base
 82 and subgrade layer [Miura et al., 1986; Brown, 1996; Gräbe and Clayton, 2009; Inam et al.,
 83 2012; Ishikawa et al., 2011, 2019b; Lin et al., 2019a]. This is because the conventional rutting

84 models are mainly built on traditional repeated loading triaxial test with constant confining
85 pressure and no principal stress axis rotation.

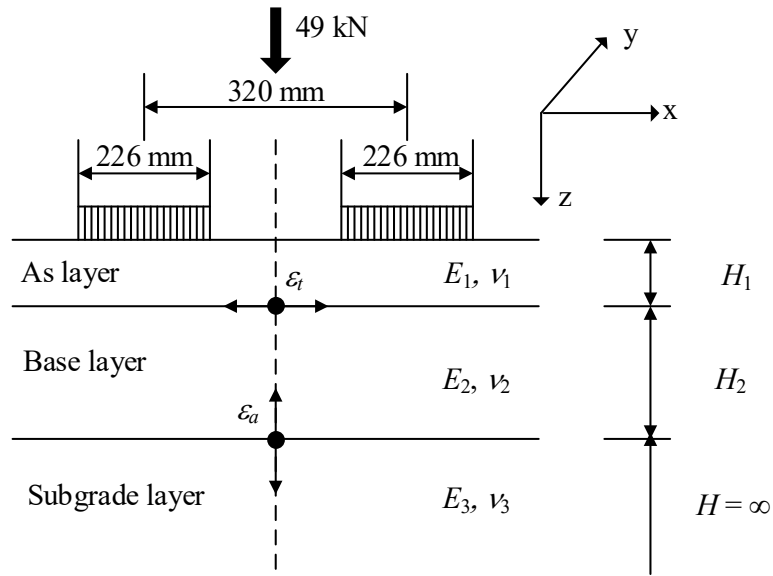
86 Consequently, to overcome aforementioned limitations, this study modified the present Japa-
87 nese pavement design method through two main aspects: (1) Replacing constant elastic modu-
88 lus of base and subgrade layer to resilient modulus related to stress states and complex climate
89 conditions, which are defined as the combination of fluctuating water content and freeze-thaw
90 action. To be precise, Ishikawa et al. [2019a] and Lin et al. [2020] studied the synergistic effect
91 between water content and freeze-thaw action, named as climate effect, on the base course and
92 subgrade materials. This study combined these research results to determine the base and sub-
93 grade layer moduli with complex water content and freeze-thaw conditions. (2) Modifying rut-
94 ting failure criterion by considering generally used MEPDG model and also the effect of prin-
95 cipal stress axis rotation. To be precise, this study modified the structure of present rutting
96 model referring to MEPDG rutting model. Furthermore, the amplification of permanent defor-
97 mation caused by PSAR is examined through laboratory test results. Such effect caused by
98 PSAR was also used to modify the structure of rutting failure criterion in this study. This study
99 specially focuses on the pavement life against rutting since modification of the fatigue cracking
100 model is done by previous researches [Maruyama et al., 2006, 2008].

101 **2. Applicability of present Japanese pavement design method**

102 2.1 Present Japanese pavement design method

103 Japanese pavement design method [JRA, 2006] provides rutting and fatigue cracking failure
104 criteria, as shown in Eqs. (3) to (5) and (6) to (13), to calculate allowable loading number of

105 equivalent 49-kN wheel loads against rutting (N_{fs}) and fatigue cracking (N_{fa}). These allowable
 106 loading numbers are calculated by a theoretical design method, also known as AI model, [As-
 107 phalt Institute, 1982] using a simplified three-layers model which consists of asphalt mixture
 108 layer (hereafter referred to as the “As layer”), base layer, and subgrade layer as shown in Fig.
 109 1.



110

111 Fig. 1 Three-layers model for allowable loading number calculation.

112
$$N_{fs} = \beta_{s1} \cdot \{1.365 \times 10^{-9} \cdot \varepsilon_a^{-4.477 \cdot \beta_{s2}}\} \quad (3)$$

113
$$\beta_{s1} = 2134 \quad (4)$$

114
$$\beta_{s2} = 0.819 \quad (5)$$

115
$$N_{fa} = \beta_{a1} \cdot C \cdot \{6.167 \times 10^{-5} \cdot \varepsilon_t^{-3.291 \cdot \beta_{a2}} \cdot E_1^{-0.854 \cdot \beta_{a3}}\} \quad (6)$$

116
$$C = 10^M \quad (7)$$

117
$$M = 4.84 * \left(\frac{VFA}{100} - 0.69\right) \quad (8)$$

118
$$\beta_{a1} = K_a * \beta_{a1}' \quad (9)$$

$$119 \quad K_a = \begin{cases} \frac{1}{8.27 \times 10^{-11} + 7.83 \cdot e^{-0.11 H_a}}, & H_1 < 0 \\ 1, & H_1 \geq 0 \end{cases} \quad (10)$$

$$120 \quad \beta_{a1}' = 5.229 \times 10^4 \quad (11)$$

$$121 \quad \beta_{a2} = 1.314 \quad (12)$$

$$122 \quad \beta_{a3} = 3.018 \quad (13)$$

123 where β_{s1} , β_{s2} , β_{a1} , β_{a2} , and β_{a3} are the compensation rates for AI failure criteria based on the
 124 actual situation of Japanese pavement; C is the material parameter; M is a factor relates the VFA
 125 to C ; VFA is Voids Filled with Asphalt; K_a is a correction factor, which relates to the thickness
 126 of asphalt mixture, H_1 . ε_a is the compressive strain on the top surface of the subgrade layer; ε_t
 127 is the tensile strain on the lower surface of the As layer.

128 ε_a and ε_t are determined through multi-layers model, which involves elastic moduli (E) and
 129 Poisson's ratio (ν) of each layer, built in General Analysis of Multi-layered Elastic Systems
 130 (GAMES) [Maina and Matsui, 2004] as shown in Fig 1. In present Japanese pavement design
 131 method, elastic moduli of As layer (E_1) changes with temperature as shown in Eqs. (14) and
 132 (15), while the elastic moduli of base layer (E_2) and subgrade layers (E_3) are constant through-
 133 out a whole year since lacking investigation of how water content, freeze-thaw, or stress states
 134 influence E_2 and E_3 .

$$135 \quad E_1 = -278.4M_p + 10930 \quad (14)$$

$$136 \quad M_p = M_a \left[1 + \frac{2.54}{h_1 + 10.16} \right] - \frac{25.4}{9(h_1 + 10.16)} + \frac{10}{3} \quad (15)$$

137 where M_p is the monthly mean temperature of asphalt mixture at depth of h_1 ($^{\circ}\text{C}$); M_a is monthly
 138 mean air temperature ($^{\circ}\text{C}$); h_1 is the depth equals to one-third of the height of asphalt mixture
 139 (cm).

140 Consequently, monthly representative E_1 and constant E_2/E_3 are used to calculate allowable

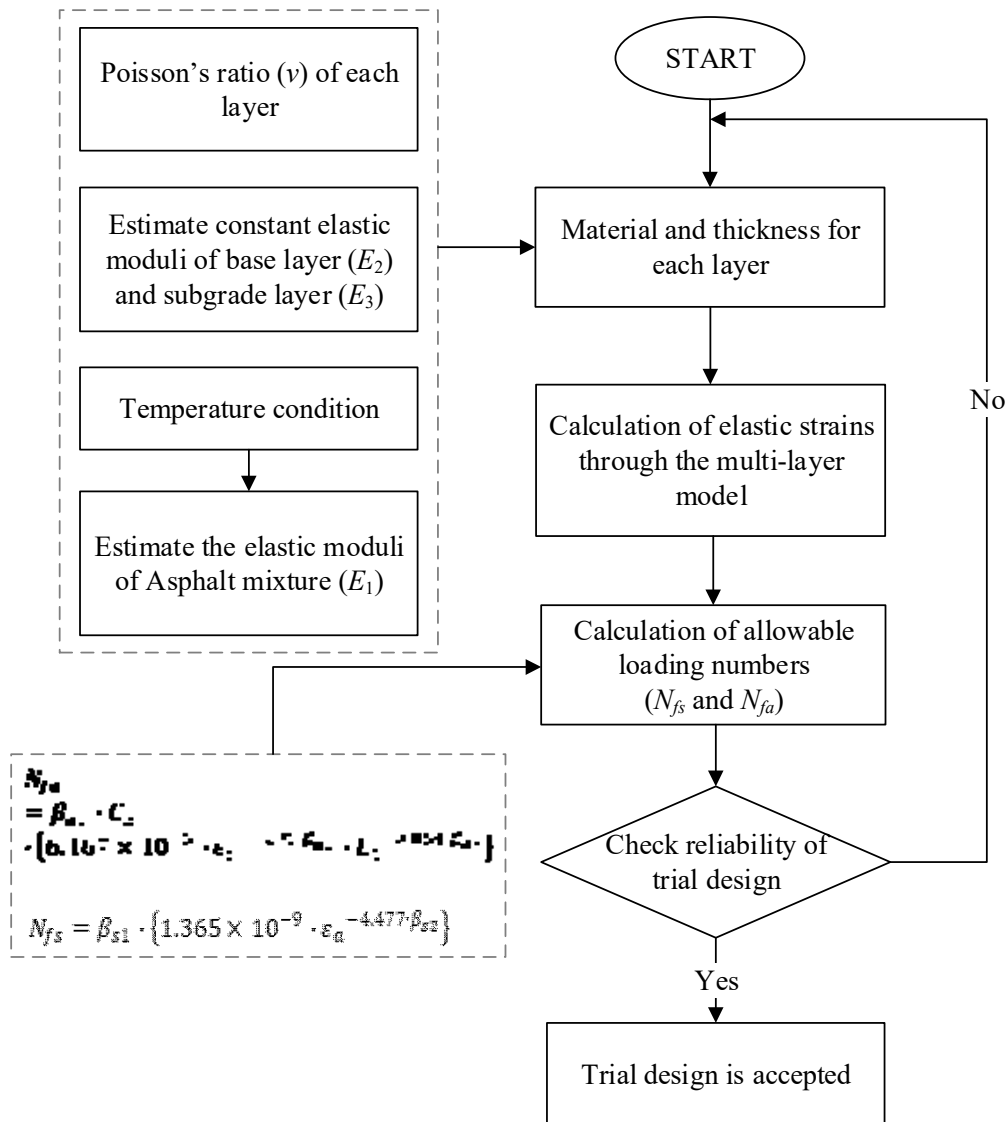
141 loading number under monthly average temperature condition, $N_{fs,i}$ and $N_{fa,i}$. $i=1\sim 12$. Failure

142 loading number $N_{fs,d}$ or $N_{fa,d}$ is calculated through Eqs. (16) and (17).

143
$$N_{f,d} = \frac{1}{D_a} \tag{16}$$

144
$$D_a = \frac{1}{12} \sum_{i=1}^{12} \frac{1}{N_{f,i}} \tag{17}$$

145 As a result, Fig. 2 illustrates the sequence in current Japanese flexible pavement design guide.



146

147 Fig. 2 Sequence in current Japanese flexible pavement design guide.

148 2.2 Test pavement structures

149 Civil Engineering Research Institute for Cold Region (CERI) designed and constructed eight

150 test pavements in Hokkaido [Maruyama et al., 2006]. Fig. 3 illustrates the structures and length

151 of each test pavement. All eight pavement structures consist of asphalt mixture, base layer, and
 152 subgrade layer with multiple materials and thickness. Four types of hot mixed asphalt mixtures
 153 are used in test pavement. Fine-graded asphalt mixture has a 0 - 13 mm aggregate gradation
 154 distribution (hydrated lime, sea sand, and crushed rock). Middle-graded asphalt mixture has the
 155 same range of gradation distribution but more coarse aggregate. Coarse-graded and stabilized
 156 asphalt mixture have a 0 - 20 mm and 0 - 30 mm gradation distribution separately. Two types
 157 of base layer material (Andesite) are used as C-40, crusher-run with maximum 40 mm gradation
 158 distribution, and C-80, anti-frost crusher-run with maximum 80 mm gradation distribution. The
 159 subgrade material is a sandy soil according to Unified Soil Classification System [ASTM, 2011],
 160 named as Tomakomai soil, composed of 8% clay, 13% silt, 51% sand, 28% gravel.

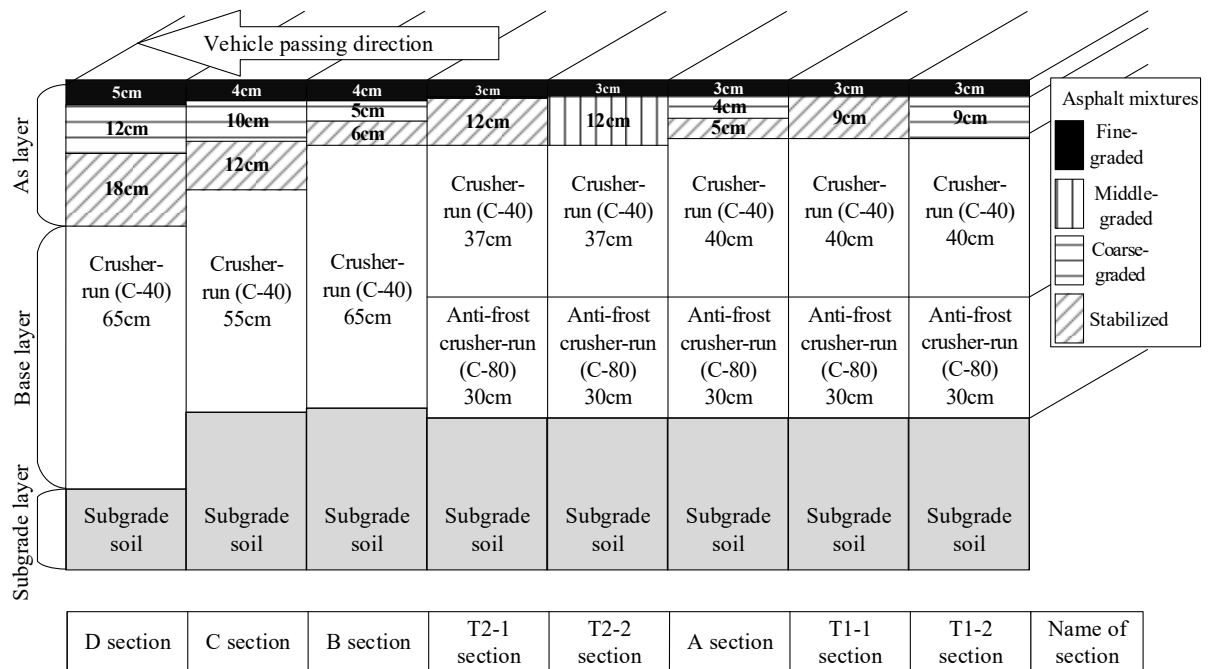


Fig. 3 Test pavement structures.

2.3 Traffic volume observation

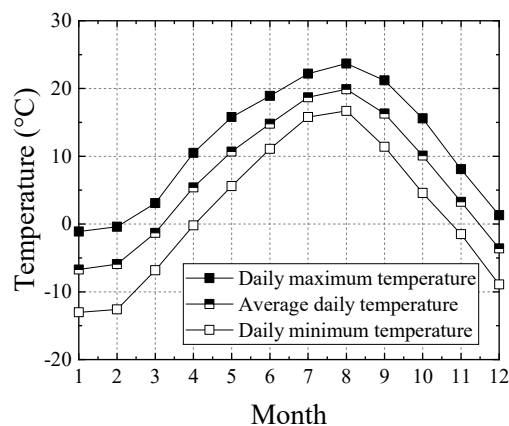
CERI observed traffic volume of test pavement during the whole life (from 1990 to 2004). Total

traffic volume, that is average annual daily vehicle (car and truck) number in one lane, is 4974

166 per day per lane. Truck volume, that is average annual daily truck number in one lane, is 1714
167 per day per lane. Wheel loads for all vehicles are in accordance with the normal distribution
168 that ranges from 15 to 80 kN. As Japanese pavement design method calculates the allowable
169 number of equivalent 49-kN wheel loads against rutting and fatigue cracking. CERI transferred
170 the traffic volume to a 49-kN wheel loads number as 2398 per day per lane during the whole
171 life of test pavement.

172 2.4 Climate data

173 Climate data are collected from Automated Meteorological Data Acquisition System (AMe-
174 DAS) [Japan Meteorological Agency]. Fig. 4 plots the monthly average value of daily temper-
175 atures during the whole life from 1990 to 2004. These climate data are used to determine the
176 stiffness of the asphalt layer in current Japanese pavement design method through Eqs. (14)
177 and (15). Besides, the monthly representative temperature is also used in modified design
178 method to determine the frost-penetration depth, which highly relates to the stiffness of base
179 and subgrade layer as frozen soil has a much larger stiffness. Determination of variant base and
180 subgrade layer stiffness related to climate condition will be introduced in latter part.



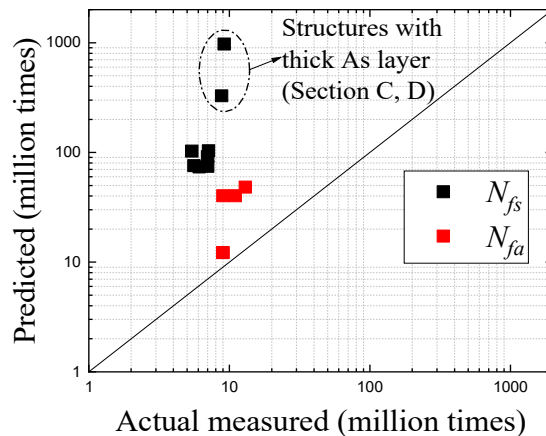
181

182

Fig. 4 Monthly average value of daily temperatures.

183 2.5 Predicted life with present Japanese pavement design method

184 To predict the life of eight test pavements, all test pavements are simplified to three-layers
185 model in GAMES with layer thickness shown in Fig. 3. E_1 is determined through Eqs. (14) and
186 (15) and monthly representative air temperatures shown in Fig. 4. Constant stiffness of base
187 layer (E_2) and subgrade layer (E_3) through the year is set as 265MPa and 76 MPa referring to
188 previous research [Maruyama et al., 2008]. Poisson's ratio of As layer, base layer, and subgrade
189 layer are set as 0.35, 0.35, and 0.4 separately, which come from Japanese pavement design
190 method recommend values. Fig. 5 compared predicted N_{fs} and N_{fa} through Eqs. (3) to (5) and
191 (6) to (13) with actual measured failure loading number. From Fig.5, it is recognized that, pre-
192 sent AI model over-estimates the pavement life, especially pavement life against rutting. Be-
193 sides, prediction bias is much larger for pavement structures with thick As layer refer to two
194 dots circled by dash line in Fig. 5. Such over-estimation is attributed to the drawbacks of Japa-
195 nese pavement design method discussed in Introduction part.



196

197 Fig. 5 Predicted pavement life through present Japanese pavement design method.

198 **3. Resilient modulus under various climate conditions and different stress states**

199 3.1 Climate effect on resilient modulus

200 3.1.1 Water content fluctuation

201 Climate effect in this study refers to the synergistic effect between water content and freeze-
202 thaw action on the resilient modulus of base course and subgrade materials and pavement life.

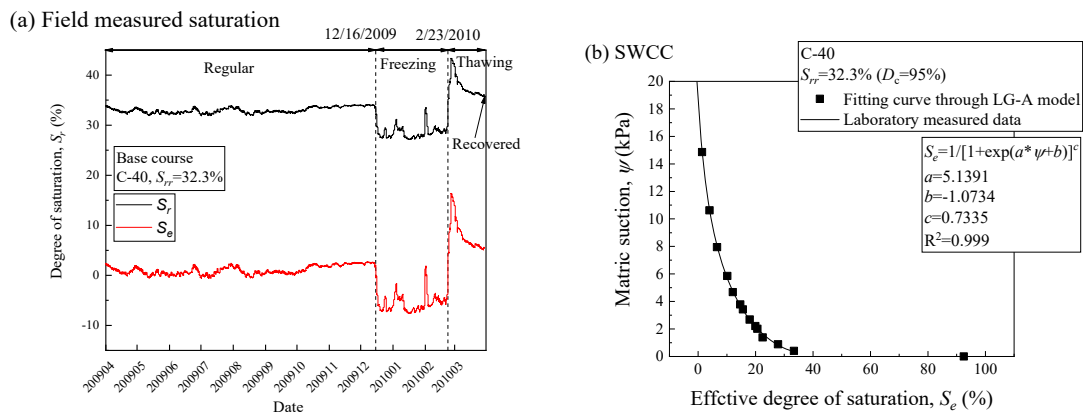
203 The universal model (Eq. (1)) cannot reflect the effect of water content. To overcome such
204 shortcoming, several modified models [Cary and Zapata, 2011; Liang et al., 2008; Ng et al.,
205 2013] are proposed based on the universal model to capture the effect of water content on re-
206 siliant modulus. Within these models, Ng model shown in Eq. (18) adds an independent stress
207 state variable that incorporates matric suction effects into the universal model and shows good
208 applicability on predicting resilient modulus of unsaturated unbound granular materials through
209 the relatively higher coefficient of determination (R^2) value than other models [Han and Vana-
210 palli, 2016]. Monthly representative E_2 and E_3 are estimated through Ng model (Eq. (18)), field-
211 measured data of water content, and SWCC of base course material and subgrade material.

$$212 \quad M_r = k_1 p_a \left(\frac{\theta}{p_a} \right)^{k_2} \left(\frac{\tau_{oct}}{p_a} + 1 \right)^{k_3} \left(\frac{\psi}{\sigma_{net}} + 1 \right)^{k_4} \quad (18)$$

213 where k_1, k_2, k_3, k_4 are regression constants; p_a is atmospheric pressure and set as 101 kPa; θ is
214 bulk stress; τ_{oct} is octahedral shear stress; σ_{net} is net mean stress (kPa), defined as $[\theta/3 - u_a]$; ψ is
215 matric suction (kPa).

216 Matric suction, ψ in Eq. (18), is determined by combining SWCC and measured long-term field
217 measurement of degree of saturation. SWCC of C-40, composed material for base layer, and
218 long-term field measured water content of base layer are plotted in Fig. 6. The effective degree
219 of saturation, S_e , of base layer illustrated as the red line in Fig. 6 (a) was calculated by using a
220 residual degree of saturation, S_{rr} , of 32.3%, which was determined through the SWCC measured

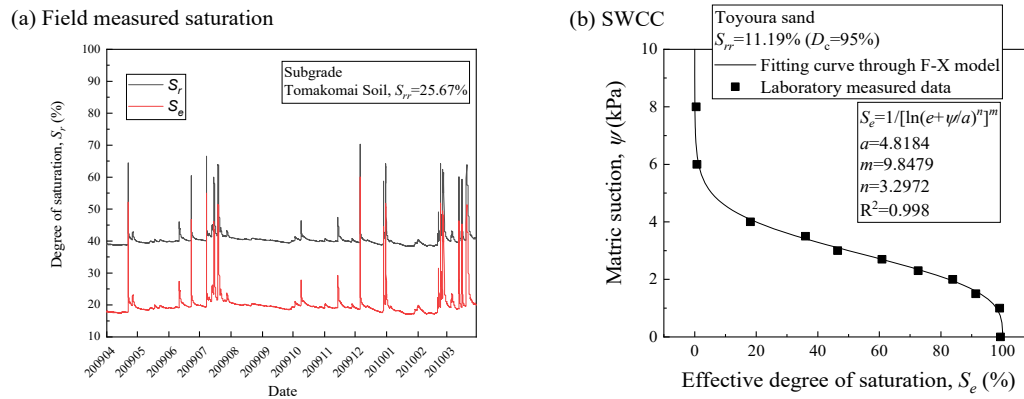
221 in laboratory water retentivity test and LG-A model [Mori et al., 2009]. Monthly average S_e is
 222 selected to determine monthly matric suction of base layer. Then, monthly representative E_2 is
 223 estimated with these monthly matric suction values. It is noted that S_r during freezing season is
 224 lower than residual S_r and S_e during freezing season is consequently lower than zero. This is
 225 due to functional features of the soil moisture sensor used in the measurement. For this reason,
 226 unrealistic measured low water content during freezing season is not used. The water content
 227 just before freezing is used as representative water content for freezing season.



228
 229 Fig. 6 (a) Long-term field measurement of base layer water content and (b) SWCC of C-40.

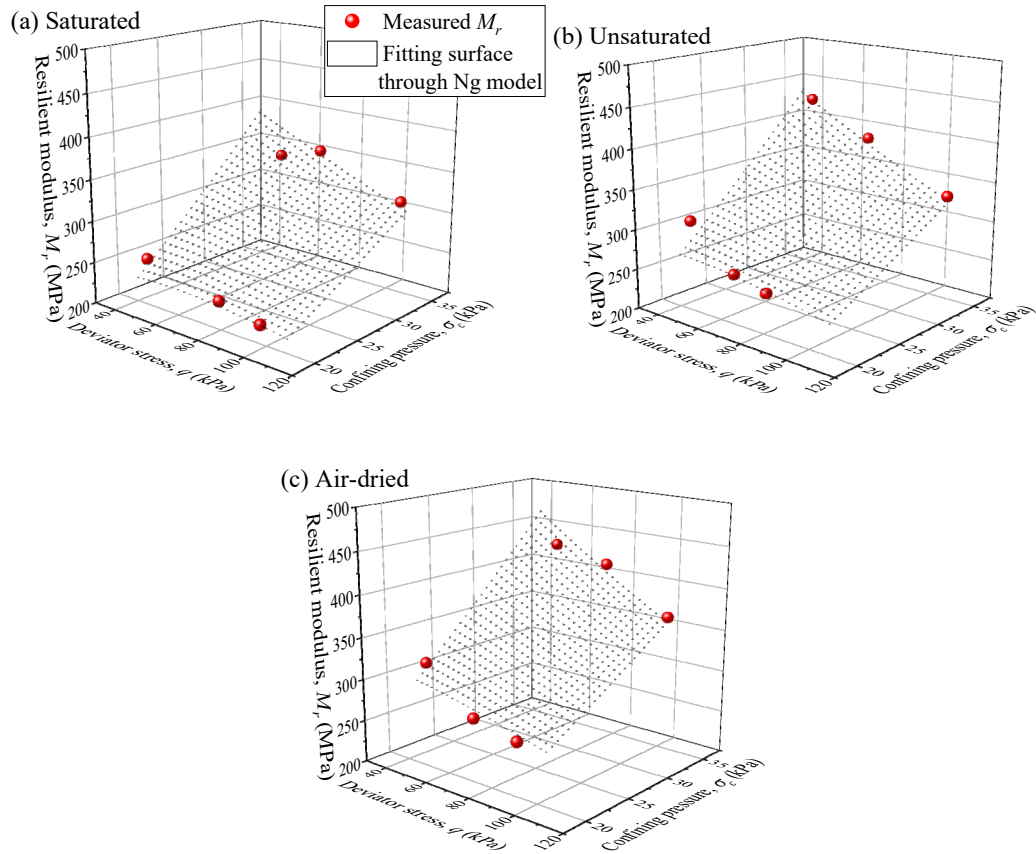
230 For subgrade layer, it is composed of Tomakomai soil. As the mechanical properties like resil-
 231 ient modulus of Tomakomai soil is under investigation and the test method of suction-controlled
 232 freeze-thaw MR test still needs verification, this study uses Toyoura sand, the standard test
 233 material, to verify newly developed test method and represent the subgrade material to check
 234 the climate effect on pavement life. It is assumed that effective degree of saturation, S_e , would
 235 be same in Toyoura sand subgrade and Tomakomai soil subgrade under same climate condition.
 236 S_e of subgrade layer illustrated as the red line in Fig. 7 (a) was calculated by using a residual
 237 degree of saturation (S_{rr}) of 25.67%, which was determined through the SWCC estimated with
 238 grain-size distribution of Tomakomai soil [Fredlund et al., 2002]. Consequently, monthly

239 average S_e is selected to determine matric suction, ψ in Eq. (18), of subgrade layer in each
 240 month through laboratory measured SWCC of Toyoura sand and fitting curve through Fred-
 241 lund-Xing model [Fredlund and Xing, 1994].



242
 243 Fig. 7 (a) Long-term field measurement of subgrade layer water content and (b) SWCC of
 244 Toyoura sand.

245 The value of constants, k_1 to k_4 , in Ng model (Eq. (18)) are determined through regression
 246 analysis on resilient modulus test results of C-40 and Toyoura sand with variant water contents.
 247 Resilient modulus of C-40 with three water contents, air-dried ($S_r=8.2\%$), unsaturated
 248 ($S_r=36.7\%$), saturated ($S_r=100\%$), are determined through medium-size triaxial apparatus.
 249 More details about the apparatus and test procedure could be found in the previous study [Ishi-
 250 kawa et al., 2019a]. Resilient modulus of Toyoura sand with two water contents, unsaturated
 251 ($S_r=40\%$), saturated ($S_r=100\%$), are determined through freeze-thaw triaxial apparatus. More
 252 details about the apparatus and test procedure could be found in the previous study [Lin et al.,
 253 2020]. Consequently, Fig. 8 and 9 show the laboratory measured resilient modulus of C-40 and
 254 Toyoura sand and corresponding fitting surface through Ng model respectively. Table 1 sum-
 255 marized the value of constants, k_1 to k_4 , in Ng model for C-40 and Toyoura sand.

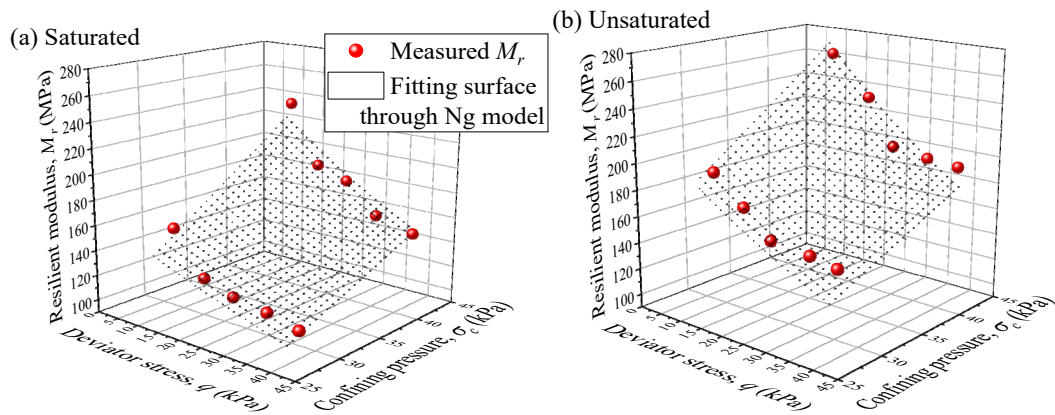


256

257

258

Fig. 8 Resilient modulus of C-40 under different water contents.



259

260

Fig. 9 Resilient modulus of Toyoura sand under different water contents.

261 Table 1. Value of regression constants.

	k_1	k_2	k_3	k_4	R^2
C-40	3.042	0.886	-1.696	1.076	0.939
Toyoura sand	2.103	1.065	-4.843	2.74	0.949

262

θ , τ_{oct} , and σ_{net} in Eq. (18) for base layer and subgrade layer are determined with a principal

263 stress ratio equals to 4 under 10 and 5 kPa confining pressure respectively. It is noted that this
 264 stress condition was selected so that M_r at normal season matches layer stiffness determined in
 265 previous research [Maruyama et al., 2008]. Consequently, Table 2 shows the monthly repre-
 266 sentative base and subgrade layer moduli considering fluctuating water contents estimated
 267 through Ng model.

268 Table 2 Monthly representative layer moduli considering fluctuating water contents

Name	Elastic moduli (MPa)											
	Jan	Feb	Mar	Apr	May	Jun	Jul	Aug	Sep	Oct	Nov	Dec
Base layer, E_2	217	209	143	193	195	195	174	185	195	191	189	208
Subgrade layer, E_3	77	75	61	76	76	71	69	76	76	76	76	75

269 3.1.2 Freeze-thaw action

270 When considering the synergistic effect between freeze-thaw action and seasonal fluctuation in
 271 water content on the stiffness of base and subgrade layer, the monthly representative elastic
 272 moduli were divided into three types of seasonal E values (E for freezing season, thawing sea-
 273 son, and regular season except for freezing and thawing seasons) for the simplicity of the pave-
 274 ment life analysis.

275 Since there is no freeze-thaw effect during the regular season, the E value for the regular season
 276 is estimated by Ng model as shown in Eq. (18) in a same way introduced in last section.

277 The E_2 and E_3 value for freezing season is set as 600 MPa and 200 MPa separately, according
 278 to back analysis of FWD test results [Ishikawa et al., 2019a]. In addition, this study assumes
 279 that when the average frost-penetration depth for the month gets into the base or subgrade layer
 280 regardless of deep or shallow, the E increases due to freezing. Here, the average frost-penetra-
 281 tion depth (z) was calculated by substituting the freezing index calculated from the daily mean
 282 air temperatures measured by AMeDAS into the modified Berggren formula [Aldrich Jr, 1956]

283 shown below:

$$284 \quad z = \alpha \sqrt{\frac{172800F}{(L/\lambda)_{eff}}} \quad (19)$$

285 where α is a correction coefficient; F is a freezing index which is the average air temperature
286 during freezing season multiplied by its duration in days; $(L/\lambda)_{eff}$ is an effective ratio of L to λ ;
287 L is the latent heat of soil; λ is a thermal conductivity of the soil.

288 The E value for thawing season stands for the average value between the moduli just after
289 thawing, corresponds to the highest water content during thawing season, and the moduli at the
290 end of thawing season, corresponds to the lowest water content during thawing season. The E
291 value during thawing season is estimated by modified Ng model (Eq. (20)), which is proposed
292 by Lin et al. [2020], with considering climate effect, F_{clim} . By adding new parameter F_{clim} into
293 Ng model as shown in Eq. (20), modified Ng model captures the complex climate effect. The
294 E value at the end of thawing season is estimated through Eq. (18) since the effect of freeze-
295 thaw is excluded.

$$296 \quad M_r = F_{clim} \cdot k_1 \cdot p_a \left(\frac{\theta}{p_a}\right)^{F_{clim} \cdot k_2} \left(\frac{\tau_{oct}}{p_a} + 1\right)^{F_{clim} \cdot k_3} \left(\frac{\psi}{\sigma_{net}} + 1\right)^{F_{clim} \cdot k_4} \quad (20)$$

297 Except modified Ng model, Liang model [Liang et al., 2008] is another approach to estimate
298 resilient modulus with changing stress states like bulk stress, octahedral shear stress, and matric
299 suction. Eqs (21) and (22) show the Liang model. The most difference between Liang model
300 and Ng model is that the former one incorporates the matric suction into applied bulk stress,
301 while the latter one extends the independent stress state variable. To capture the freeze-thaw
302 effect on resilient modulus, Ishikawa et al. [2019a] modified Liang model (Eq. (23)) is built by
303 adding a reduction factor, $f(N_f, \theta)$, on Eq. (21). $f(N_f, \theta)$ uses number of freeze-thaw process cycles
304 (N_f) and volumetric water content (θ) for the sample as explanatory variables.

305
$$M_R = k_1 p_a \left(\frac{\theta_b + \chi \psi}{p_a} \right)^{k_2} \left(\frac{\tau_{oct}}{p_a} + 1 \right)^{k_3} \quad (21)$$

306
$$\chi = \left(\frac{(u_a - u_w)_b}{\psi} \right)^{0.55} \quad (22)$$

307
$$M_R = f(N_f, \theta) \cdot k_1 p_a \left(\frac{\theta_b + \chi \psi}{p_a} \right)^{k_2} \left(\frac{\tau_{oct}}{p_a} + 1 \right)^{k_3} \quad (23)$$

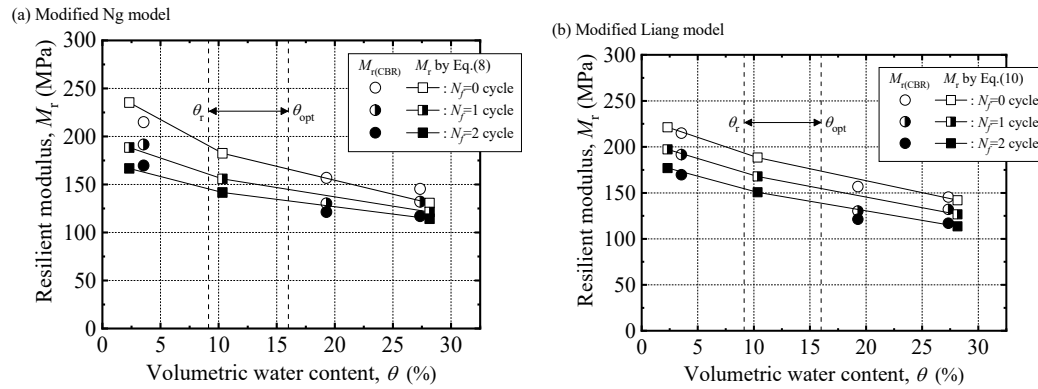
308 where θ_b is bulk stress; $(u_a - u_w)_b$ is air entry value.

309 For base course material, both Ng model (Eq. (18)) and Liang model (Eq. (21)) have high R^2
310 value on the unfrozen C-40 material as shown in Table 3. The applicability of modified Ng
311 model (Eq. (20)) and modified Liang model (Eq. (23)) on freeze-thawed C-40 are checked by
312 comparing estimated M_r with freeze-thawed $M_{r(CBR)}$. Freeze-thawed $M_{r(CBR)}$ is detected with a
313 freeze-thaw CBR (California Bearing Ratio) test apparatus which is based on a general CBR
314 test apparatus and improved to reproduce in a laboratory environment the freeze-thaw history
315 expected to be applied to the base course materials in the in-situ pavement structures. A series
316 of freeze-thaw CBR tests for C-40 was conducted under three different water contents, air-dried
317 ($S_r=12.3\%$), unsaturated ($S_r=67\%$), saturated ($S_r=95\%$), along with three different patterns of
318 freeze-thaw history, no freeze-thaw, once freeze-thaw, and twice freeze-thaw, in order to exam-
319 ine the effects of freeze-thaw action and water content on the frost-heave and bearing-capacity
320 characteristics of base course material. More details about the freeze-thaw CBR test apparatus
321 and procedure could be found in the previous study [Ishikawa et al., 2019a]. Fig. 10 shows the
322 $M_{r(CBR)}$ and estimated M_r with Eq. (20) and (23). It is noted that, both models can give reason-
323 able predicted M_r and also capture the decreasing M_r with more freeze-thaw numbers and higher
324 water contents. Table 3-1 also shows the R^2 value, F_{clim} , and $f(N_f, \theta)$ of modified Ng model (Eq.
325 (20)) and modified Liang model (Eq. (23)) on freeze-thawed $M_{r(CBR)}$. It is noted that when con-
326 ducting regression analysis for freeze-thawed test, only F_{clim} and $f(N_f, \theta)$ are variant and k_1 to k_4

327 are fixed to check the validity of newly added parameters. Both models show high accuracy
 328 ($R^2 > 0.9$).

329 Table 3. Applicability of Modified Liang model and Modified Ng model on C-40

		k_1	k_2	k_3	k_4	F_{clim}	$f(N_f, \theta)$	R^2
U	Ng model	3.042	0.886	-1.696	1.076	—	—	0.939
	Liang model	4.861	1.525	-2.092	—	—	—	0.950
FT ($N_f=1$)	modified Ng model	3.042	0.886	-1.696	1.076	0.749	—	0.921
	modified Liang model	4.861	1.525	-2.092	—	—	0.891	0.991
FT ($N_f=2$)	modified Ng model	3.042	0.886	-1.696	1.076	0.644	—	0.968
	modified Liang model	4.861	1.525	-2.092	—	—	0.800	0.998



330

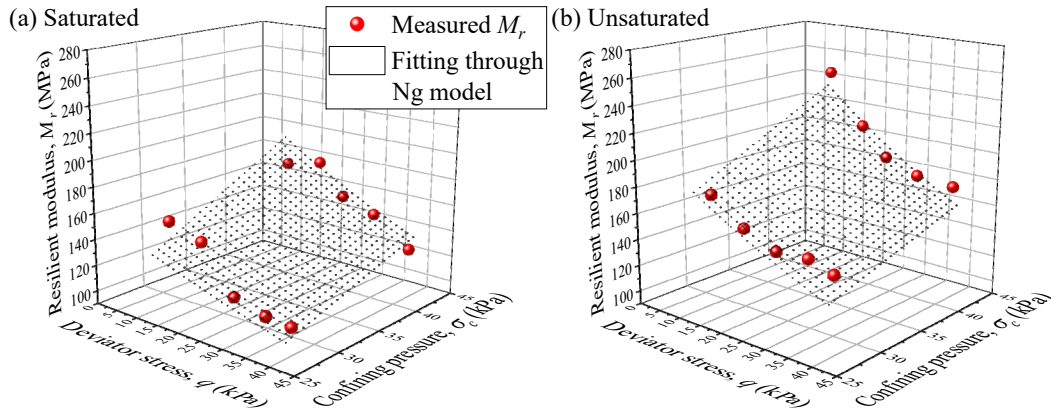
331 Fig. 10 Estimated M_r with (a) modified Ng model and (b) modified Liang model.

332 For subgrade material, Table 4 shows the applicability of Ng model (Eq. (18)) and Liang model
 333 (Eq. (21)) on unfrozen Toyoura sand, and the applicability of modified Ng model (Eq. (20))
 334 and modified Liang model (Eq. (23)) on freeze-thawed Toyoura sand. Freeze-thaw resilient
 335 modulus of Toyoura sand is detected with freeze-thaw triaxial apparatus which could circulate
 336 low temperature fluids in the cap, pedestal, and inner cell to control the cap, pedestal, and
 337 around temperature of specimen separately to simulate one-dimensional freeze-thaw action. A
 338 series of freeze-thaw resilient modulus tests for Toyoura sand was conducted under two differ-
 339 ent water contents, unsaturated ($S_r=40\%$), saturated ($S_r=100\%$), along with two different pat-
 340 terns of freeze-thaw history, no freeze-thaw and once freeze-thaw, in order to examine the ef-
 341 fects of freeze-thaw action and water content on the mechanical properties of subgrade

342 materials. More details about the test condition and results could be found in previous research
 343 [Lin et al., 2020]. Fig. 11 shows the freeze-thaw resilient modulus test results for Toyoura sand.
 344 It is noted that unfrozen resilient modulus test results for Toyoura sand is already plotted in Fig.
 345 9.

346 Table 4. Applicability of Modified Liang model and Modified Ng model on Toyoura sand

		k_1	k_2	k_3	k_4	F_{clim}	$f(N_f, \theta)$	R^2
U	Ng model	2.103	1.065	-4.843	2.74	—	—	0.949
	Liang model	2.396	0.979	-4.912	—	—	—	0.767
FT ($N_f=1$)	modified Ng model	2.103	1.065	-4.843	2.74	0.885	—	0.901
	modified Liang model	2.396	0.979	-4.912	—	—	0.910	0.621



347
 348 Fig. 11 Freeze-thaw resilient modulus of Toyoura sand under different water contents.
 349 When performing regression analysis for freeze-thaw test results through modified Ng model
 350 (Eq. (10)) or modified Liang model (Eq. (12)), only F_{clim} and $f(N_f, \theta)$ are variant and k_1 to k_4 are
 351 fixed to the same value obtained from regression analysis on unfrozen test results to check the
 352 validity of newly added parameters. It is recognized that Ng model shows much higher R^2 value
 353 than Liang model no matter for unfrozen or freeze-thawed C-40 and Toyoura sand. Conse-
 354 quently, this study uses modified Ng model to estimate resilient modulus of base layer and
 355 subgrade layer with fluctuating water content and various freeze-thaw histories. In addition,
 356 Table 5 shows the monthly representative base and subgrade layer moduli estimated through

357 modified Ng model with considering fluctuating water contents and freeze-thaw action.
 358 Through comparing Table 2 and 5, it is concluded the M_r increases to a high value during freez-
 359 ing season and drops further in thawing season according to the thaw weakening no matter for
 360 base or subgrade layer.

361 Table 5 Monthly representative layer moduli considering climate effect

Name	Elastic moduli (MPa)											
	Jan	Feb	Mar	Apr	May	Jun	Jul	Aug	Sep	Oct	Nov	Dec
Base layer, E_2	600	600	110	193	195	195	174	185	195	191	189	208
Subgrade layer, E_3	77	200	50	76	76	71	69	76	76	76	76	75

362 3.2 Dependency of resilient modulus on stress state

363 As discussed in introduction part, present Japanese design guide use constant elastic moduli of
 364 base layer and subgrade layer to calculate the strains under 49-kN wheel load. To overcome the
 365 limitation that unchangeable layer moduli under variant stress states caused by different layer
 366 thickness, the widely used resilient modulus in MEPDG, which changes with different stress
 367 states like deviator stress and confining pressure, is applied in this study to estimate the layer
 368 stiffness precisely. A convergence analysis of M_r is necessary to determine the reliable layer
 369 stiffness under 49-kN wheel loads since M_r affects and is conversely affected by the stress states.

370 The convergence analysis is conducted through following steps [JSCE 2015]:

- 371 1) Input E_1 , E_2^I , and E_3^I in the GAMES to obtain the stress states in base layer and subgrade
 372 layer. According to previous researches [Huang, 2004], stress states in two points shown in Fig.
 373 12 are chosen to estimate E for whole base and subgrade layer.

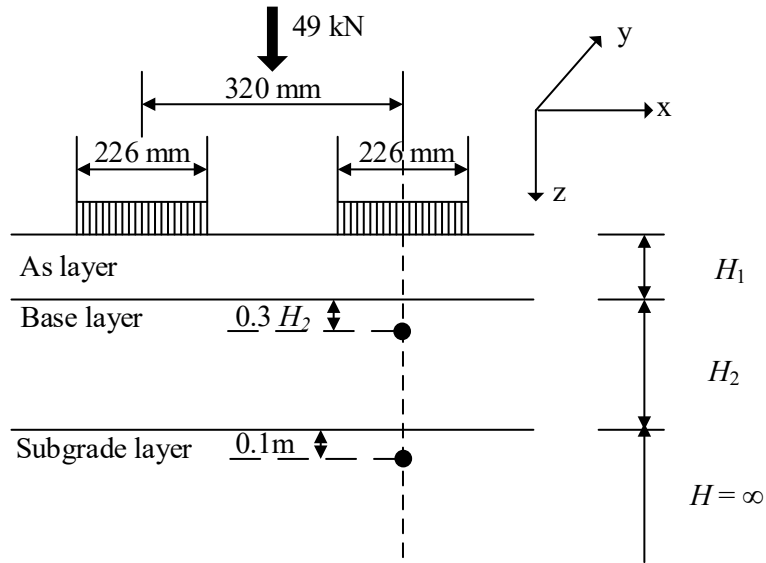


Fig. 12 Stress states calculation points in base and subgrade layer.

2) Substitute the stress states obtained in step 1 into modified Ng model to obtain new E_2^2 and

E_3^2 .

3) Step 1 and 2 are repeated until the error calculated in following equation is less than 1%.

$$e_{rr} = \frac{|E^{i-1} - E^i|}{E^i} \times 100 \quad (24)$$

where E^i and E^{i-1} is the layer modulus estimated in i th and $i-1$ th iterations.

Based on this convergence analysis sequence, Fig. 13 shows the development of estimated re-

silient modulus of base layer and subgrade layer with number of iterations in normal season

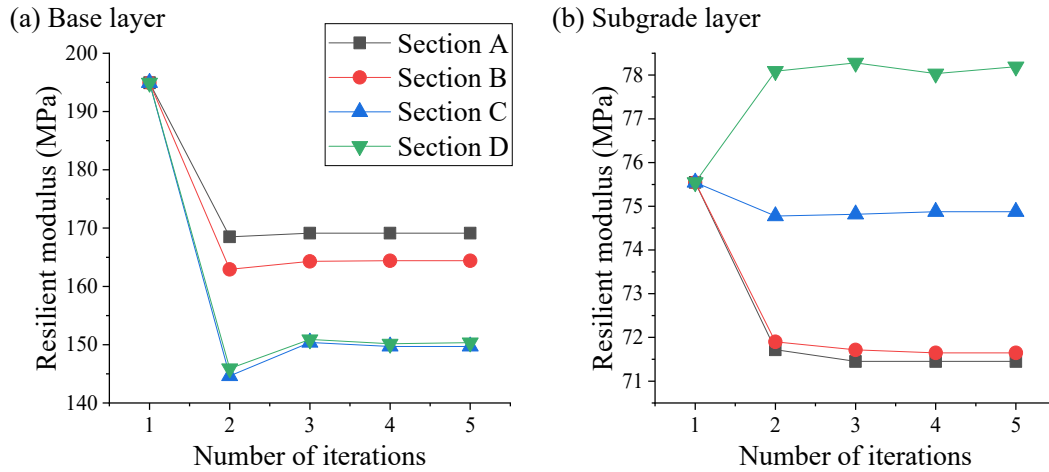
(Aug). It is noted that all moduli are stable after 2-4 iterations. Besides, convergent E_2 decreases

in all pavement sections and convergent E_3 decreases in section A, B, C while increases in

section D compared with elastic moduli without convergence analysis. Resilient moduli in other

month show similar tendency that E_2 decreases in all pavement sections and E_3 decreases in

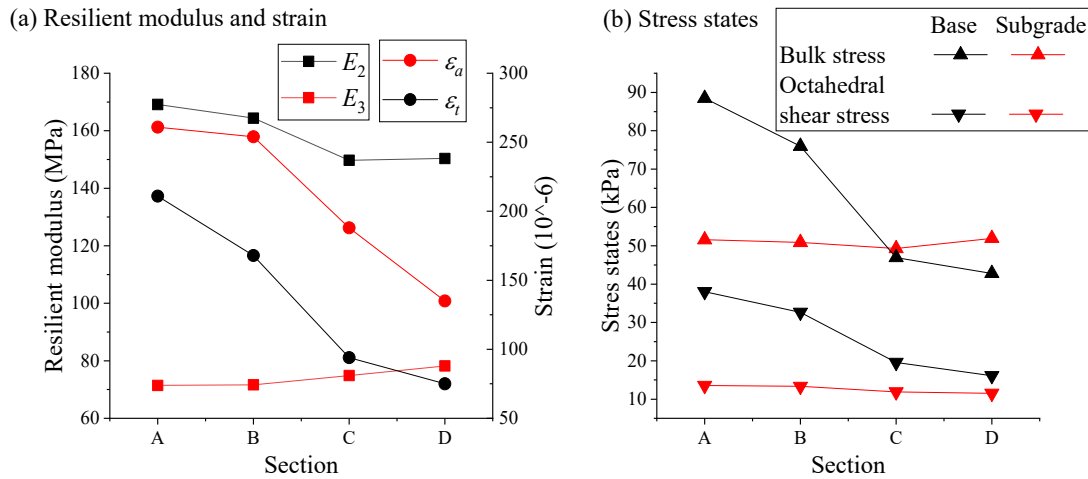
section with thin As layer while increases in section with thick As layer.



388

389

Fig. 13 Estimated resilient modulus of (a) base layer and (b) subgrade layer.



390

391

Fig. 14 (a) Resilient modulus and (b) stress states in different sections.

392 Different increasing or decreasing tendency comes from the variant stress states when pavement
 393 structures changing. To clearly discuss how pavement structures and stress states influence the
 394 resilient modulus at stable condition, Fig. 14 compares resilient modulus, strain, and stress
 395 states in different sections. Since As layer thickness increases from section A to D, it is con-
 396 cluded that E_2 decreases significantly with As layer thickness while E_3 slightly increases with
 397 As layer thickness. It is noted that Fig. 14 only show convergent resilient modulus and corre-
 398 sponding stress sates for Aug, which stands for the normal season, and that resilient modulus
 399 and corresponding stress sates for other months show the same tendency. Such tendency could

400 be attributed to the changing bulk stress (θ) and octahedral shear stress (τ_{oct}) with As layer
401 thickness, as shown in Fig 14 (b). θ has a positive effect on the M_r while τ_{oct} has a negative
402 effect. In base layer, decreasing θ with thicker As layer is more significant than decreasing τ_{oct}
403 with thicker As layer. Consequently, E_2 decreases from A to D. In subgrade layer, θ increases
404 while τ_{oct} decreases with As layer thickness. As a result, E_3 increases from A to D. Since fluctua-
405 tion of stress states in base layer is much significant than those in subgrade layer, fluctuation
406 of moduli in base layer is accordingly larger. Elastic strains (ϵ_a and ϵ_t) are also shown in Fig. 14
407 (a). It is clear that no matter compressive strain (ϵ_a), which is used in Eq. (1) to calculate N_{fs} , or
408 tensile strain (ϵ_t), which is used in Eq. (4) to calculate N_{fa} , both strains decrease with As layer
409 thickness. Such tendency is reasonable as asphalt mixture has a much larger stiffness than
410 crusher-run material and subgrade soil, and a thicker As layer improves the mechanical prop-
411 erties of the whole multi-layer elastic structure. Table 6 summarizes the convergent monthly
412 representative base/subgrade layer moduli in A section. M_r for freezing season keeps constant
413 due to freezing of soils. In this case, this study only performs the convergence analysis again
414 M_r except the freezing season.

415 Table 6 Convergent monthly representative base/subgrade layer moduli in A section.

Name	Elastic moduli (MPa)											
	Jan	Feb	Mar	Apr	May	Jun	Jul	Aug	Sep	Oct	Nov	Dec
E_2 -Water con- tent fluctua- tion	191	185	132	173	175	175	161	169	176	172	170	184
E_2 -Climate ef- fect	600	600	105	173	175	175	161	169	176	172	170	184
E_3 -Water con- tent fluctua- tion	74	73	58	74	73	69	68	72	73	73	73	73
E_3 -Climate ef- fect	77	200	40	74	73	69	68	72	73	73	73	73

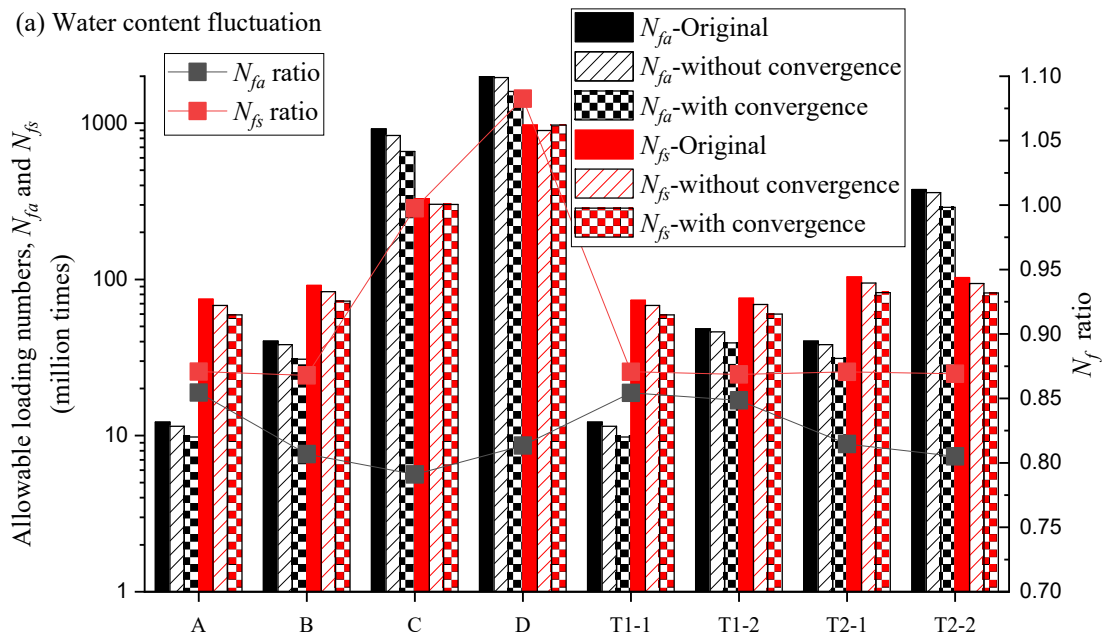
416 3.3 Influence of stress state and climate effect on pavement life

417 3.3.1 Stress state dependency

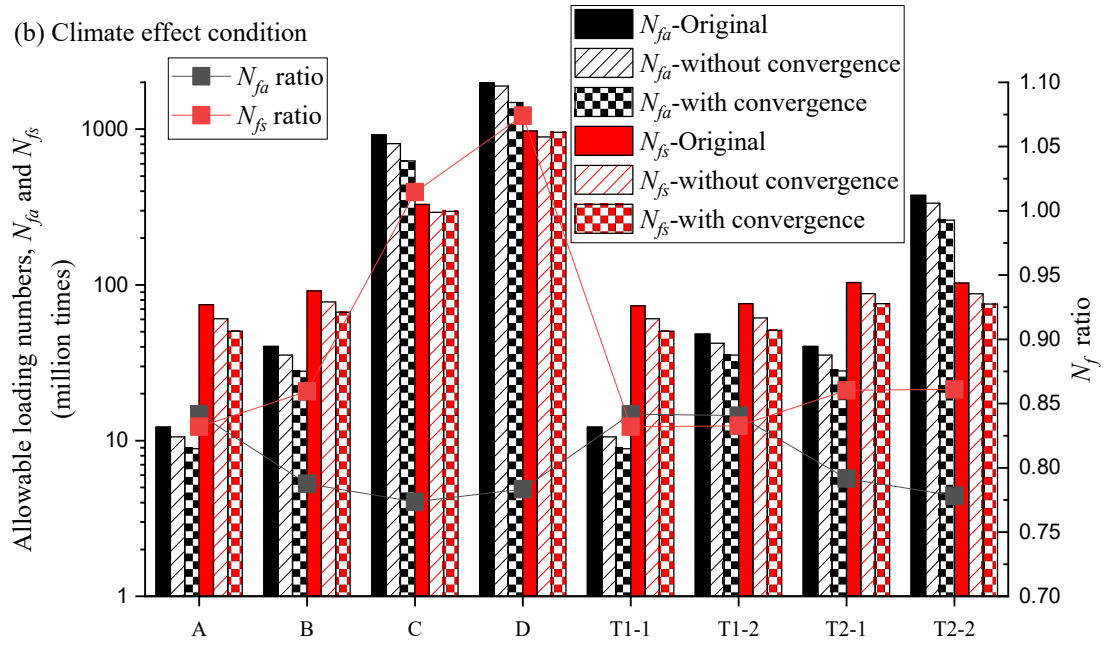
418 Fig.15 illustrates the calculated pavement life of all sections through layer moduli with and
419 without convergence analysis. The ratio of N_f with convergent E_2 and E_3 to N_f without conver-
420 gent E_2 and E_3 is also plotted here. Pavement life under water content fluctuation condition,
421 which means layer stiffness E_2 and E_3 changing with water contents, and climate condition,
422 which means E_2 and E_3 changing with water contents and freeze-thaw action, are shown in
423 Figs.15 (a) and (b) separately. N_{fa} always decreases with convergent E_2 and E_3 regardless of
424 pavement structures while N_{fs} only decreases with convergent E_2 and E_3 in pavement structures
425 with thin As layer (A, B, T1 and T2). Convergent E_2 and E_3 has a negative effect on the pave-
426 ment life against fatigue cracking and this effect is more significant in thick As layer pavement
427 structure. On the other hand, convergent E_2 and E_3 has a negative effect on the pavement life
428 against rutting when As layer is thin. Consequently, convergence analysis for layer stiffness is
429 essential when developing a mathematical flexible pavement design method with high applica-
430 bility and precision.

431 In addition, the effect of convergence analysis on pavement life is basically more significant
432 compared with effect of water content fluctuation or climate effect regardless of section struc-
433 ture. To be precise, the difference between N_f -Original, the pavement life calculated with con-
434 stant E_2 and E_3 , and N_f -without convergence is less significant than the difference between N_f -
435 without convergence and N_f -with convergence no matter the water content fluctuation (Fig.
436 15(a)) or climate effect is considered (Fig. 15(b)). The only exception that the effect of conver-
437 gence analysis is less significant than effect of water content fluctuation or climate effect is for

438 the pavement life against rutting (N_{fs}) of structure with thick As layer. For example, for section
 439 C and D, the difference between N_{fs} -Original and N_{fs} -without convergence is more significant
 440 than the difference between N_{fs} - without convergence and N_{fs} -with convergence. Such results
 441 indicate that in pavement structures such as high-standard roads, environmental condition de-
 442 pendence has a greater effect on pavement life than stress dependence and should be considered
 443 as a more significant factor. Especially in the case of Japanese pavement where rutting is more
 444 of a problem than fatigue cracking.



445



446

447 Fig. 15 Convergence analysis effect on pavement life under (a) water content fluctuation con-

448

dition (b) climate effect condition

449

3.3.2 Climate effect on pavement life

450

Figs. 16 and 17 illustrate N_{fs} and N_{fa} of eight test pavement structures under three conditions,

451

namely Original, Water content fluctuation, and Climate effect. It is noted that all pavement life

452

in water content fluctuation condition and climate condition are calculated with convergent

453

layer moduli. In other words, Figs. 16, 17 are plotted by rearranging the calculation results in

454

Fig. 15. It is obvious that N_{fs} and N_{fa} both decrease from original condition to water content

455

condition, which implies that changing E_2 and E_3 with fluctuating water content decrease pave-

456

ment life. N_{fs} and N_{fa} decrease further from water content fluctuation condition to climate con-

457

dition, which indicates that freeze-thaw action decreases pavement life further as the decreasing

458

E_2 and E_3 during thawing season has a stronger influence on the pavement life than the increas-

459

ing E_2 and E_3 during the freezing season.

460

To clearly discuss the influence of water content fluctuation, freeze-thaw action, and climate

461 effect on the pavement life, R_{Nf} for different structures are also plotted in the Figs. 16 and 17.

462 The R_{Nf} considering water content fluctuation or climate effect are determined through dividing

463 the N_f -Water content fluctuation or N_f -Climate effect by the N_f -Original, while the R_{Nf} consid-

464 ering freeze-thaw action is determined through dividing the N_f -Climate effect by the N_f -Water

465 content fluctuation. All ratios are lower than 1, indicates that influence of water content fluctu-

466 ation, freeze-thaw action, and climate effect on E_2 and E_3 all decrease the pavement life. Within

467 pavement life against rutting calculation results, R_{Nf} caused by water content, freeze-thaw ac-

468 tion, and climate effect are around 0.819, 0.931, and 0.765 separately. In other words, the N_{fs}

469 decreases 18.1% when changing E_2 and E_3 caused by water content fluctuation is considered

470 and it would further decrease 6.9% when effect of freeze-thaw action on E_2 and E_3 is also con-

471 sidered. A synergistic climate effect on E_2 and E_3 decreases N_{fs} about 23.5%. Within pavement

472 life against fatigue cracking calculation results, R_{Nf} caused by water content, freeze-thaw action,

473 and climate effect are around 0.759, 0.93, and 0.706 separately. In other words, the N_{fa} decreases

474 24.1% when changing E_2 and E_3 caused by water content fluctuation is considered and it would

475 further decrease 7% when effect of freeze-thaw action on E_2 and E_3 is also considered. A syn-

476 ergistic climate effect on E_2 and E_3 decreases N_{fa} about 29.4%. It is noted that, all these decreas-

477 ing ratios include the effect of convergence analysis discussed in previous section.

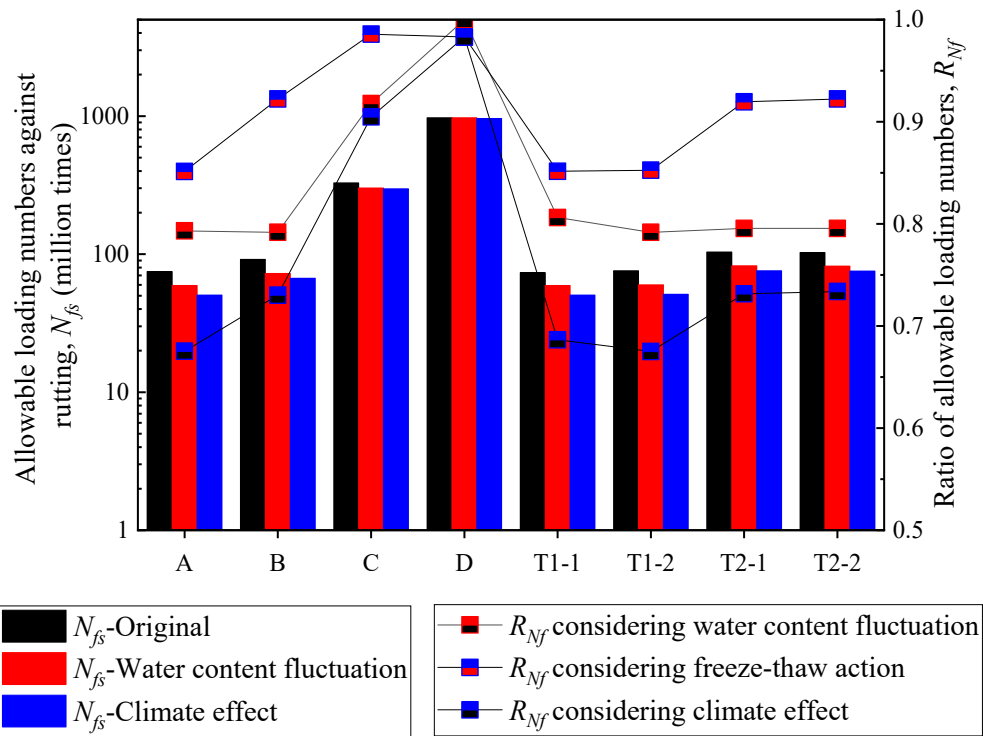
478 These results suggest that for improving the applicability and validity of the current Japanese

479 design standard, the introduction of the theoretical design method for pavement structures,

480 which can take account of the effects of the freeze-thaw actions and the concurrent seasonal

481 fluctuation in water content on the base and subgrade layer stiffness, is effective in the asphalt

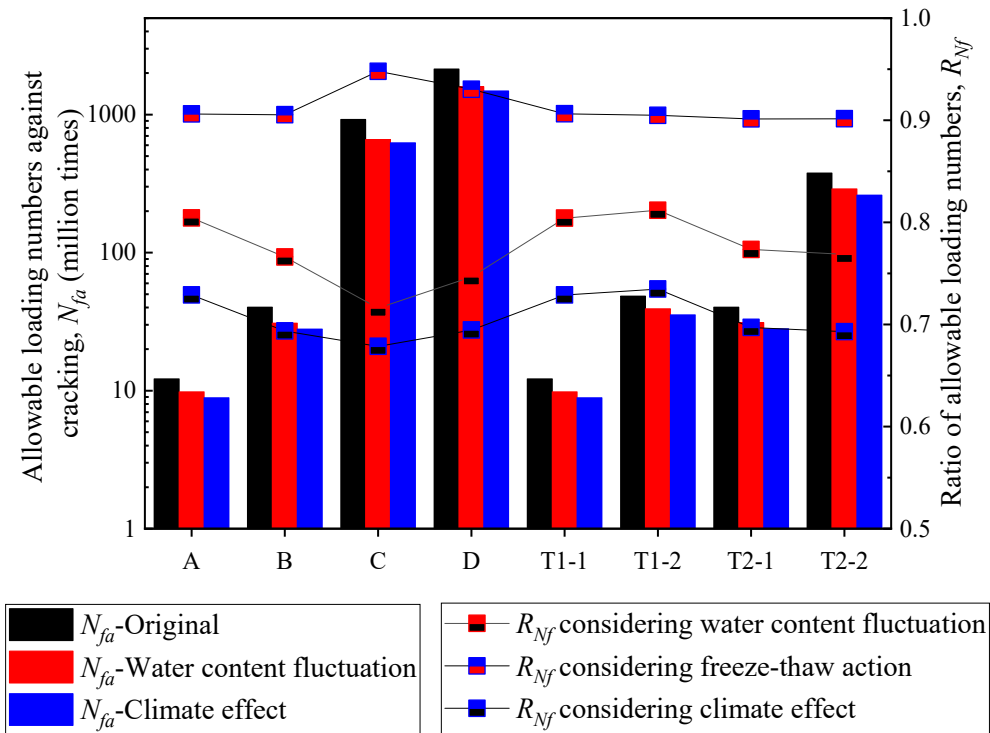
482 pavements for cold regions.



483

484

Fig. 16 N_{fs} of eight test pavement structures.



485

486

Fig. 17 N_{fa} of eight test pavement structures.

487 **4. Modification of failure criteria**

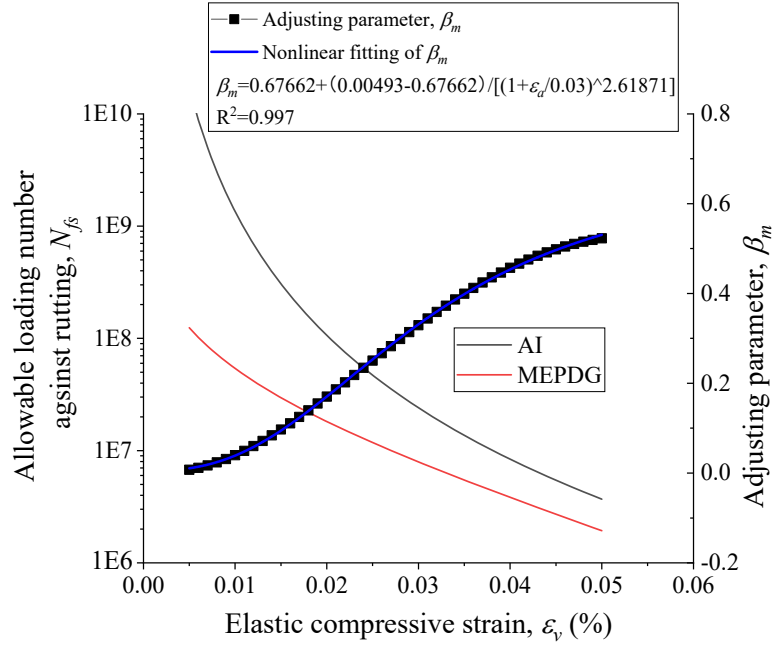
488 4.1 MEPDG rutting prediction model

489 To overcome the limitations of Japanese rutting failure criterion explained in the introduction
490 part, this section modified the structure of AI model (Eq. (3)) referring to MEPDG rutting depth
491 prediction model (Eq. (2)).

492 By applying the rutting failure threshold value in present Japanese design guide (15mm) into
493 Eq. (2), allowable loading number against rutting could be calculated through Eq. (25).

494
$$N_{fs} = \rho \cdot \left(\ln \left(\frac{\beta_{s1} k_1 \varepsilon_v h \left(\frac{\varepsilon_0}{\varepsilon_r} \right)}{15} \right) \right)^{-1/\beta} \quad (25)$$

495 Fig. 18 shows the allowable loading number against rutting through AI model (namely N_{fs} -AI)
496 and MEPDG model (namely N_{fs} -MEPDG) under various elastic compressive strain (ε_v). N_{fs} -AI
497 is much larger than N_{fs} -MEPDG when ε_a locates between 50 to 500 E-6, which is the normal
498 range for ε_a . In other words, AI model greatly overestimate the allowable loading number
499 against rutting as compared with MEPDG model. To modify the AI model based on MEPDG,
500 this study introduces an adjusting parameter, β_m , to the traditional AI model. Newly developed
501 one is named as AI-MEPDG rutting model as show in Eq. (26). β_m is calculated through divid-
502 ing N_{fs} -MEPDG by N_{fs} -AI. A logistic function is used to build the relation between β_m and ε_a ,
503 as shown in Fig. 18 and Eq. (27). Consequently, AI-MEPDG rutting model is shown in Eqs.
504 (26) and (27) to calculate allowable loading number against rutting.



505

506 Fig. 18 Allowable loading number against rutting calculated through AI and MEPDG model.

507
$$N_{fs} = \beta_m \cdot \beta_{s1} \cdot \{1.365 \times 10^{-9} \cdot \varepsilon_a^{-4.477 \cdot \beta_{s2}}\} \quad (26)$$

508
$$\beta_m = A_2 + \frac{A_1 - A_2}{1 + (\varepsilon_a / x_0)^p} \quad (27)$$

509 A_1 and A_2 : lower and upper limit of β_m and the A_1 is forced as positive value. $A_1=0.000493$;

510 $A_2=0.67672$.

511 x_0 : fitting parameter, equals to 0.03.

512 p : fitting parameter, equals to 2.61871.

513 With AI-MEPDG rutting model, the N_{fs} in climate condition is calculated and illustrated in Fig.

514 19. It is noted that, N_{fs} through AI-MEPDG rutting model in Fig. 19 is calculated with conver-

515 gent layer moduli. The tendency for the ratio of N_{fs} with convergence to N_{fs} without convergence

516 in AI-MEPDG rutting model is almost similar to that in Fig. 15. AI-MEPDG rutting model

517 gives much smaller predicted N_{fs} than AI model predicted value. However, compared with ac-

518 tual measured loading number at failure, predicted N_{fs} through AI-MEPDG rutting model are

519 still too large. Bias between predicted and actual pavement life are probably caused by

Name	sample	content	Height (mm)	density (g/cm ³)	axial stress, (σ_a) _{max} (kPa)	shear stress, ($\tau_{a\theta}$) _{max} (kPa)
FL	Toyouura sand	Oven- dried	100	1.463	72.58	0
FL	Toyouura sand	$S_r=25.6\%$	100	1.463	72.58	0
FL	Toyouura sand	$S_r=31.6\%$	100	1.463	72.58	0
FL	Toyouura sand	$S_r=46\%$	100	1.463	72.58	0
ML	Toyouura sand	Oven- dried	100	1.463	72.58	18.12
ML	Toyouura sand	$S_r=25.6\%$	100	1.463	72.58	18.12
ML	Toyouura sand	$S_r=31.6\%$	100	1.463	72.58	18.12
ML	Toyouura sand	$S_r=46\%$	100	1.463	72.58	18.12

536 It is obvious that PSAR greatly amplifies the permanent axial strain regardless of water content.

537 To quantitatively describe the amplified axial strain caused by PSAR, ratio of axial strain,

538 $(R_s)_{ave}$, is also plotted in Fig. 20. $(R_s)_{ave}$ is determined through dividing permanent axial strain

539 with PSAR to that without PSAR. Consequently, all ratios are stable around 1.90 after 180

540 loading cycles. According to previous research [Ishikawa et al., 2019b, Lin et al., 2019a], $(R_s)_{ave}$

541 could be roughly approximated by Eq. (28). In this case, the constant β_{PSAR} in Eq. (28) is deter-

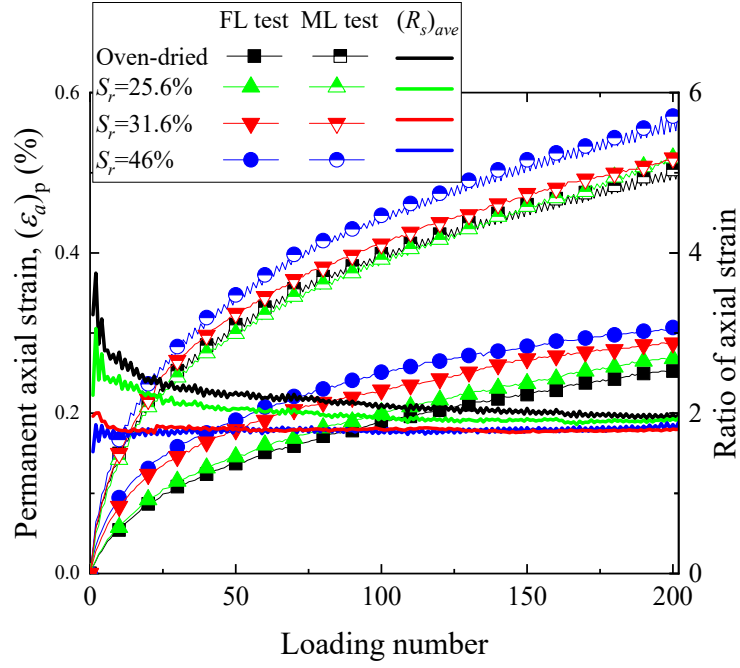
542 mined as 2.57 according to the test results that $(R_s)_{ave}$ equals to 1.9, $(\sigma_a)_{max}$ and $(\tau_{a\theta})_{max}$ are 72.58

543 kPa and 18.12 kPa respectively.

$$544 \quad (R_s)_{ave} = \exp \left(\beta_{PSAR} \frac{(\tau_{a\theta})_{max}}{(\sigma_a)_{max}} \right) \quad (28)$$

545 where $(\sigma_a)_{max}$ is maximum axial stress; $(\tau_{a\theta})_{max}$ is maximum shear stress; β_{PSAR} is material con-

546 stant.



547

548

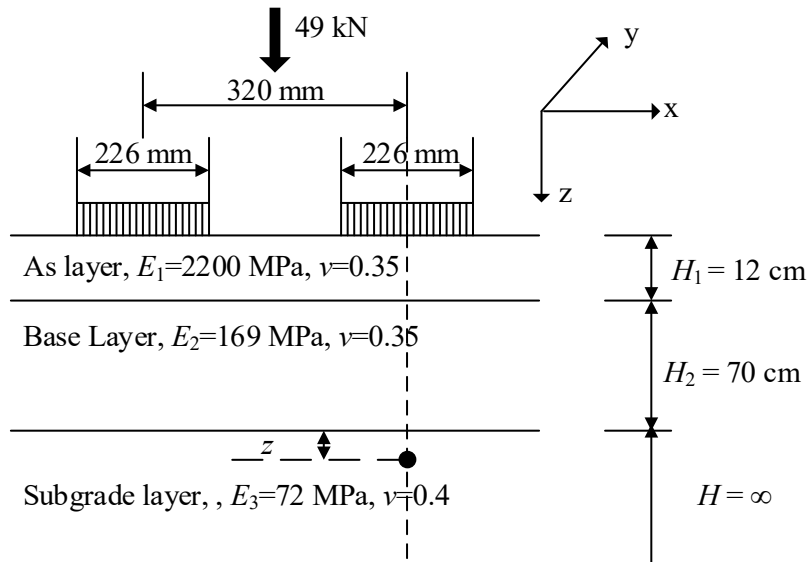
Fig. 20. Permanent axial strain of Toyoura sand.

549 As $(R_s)_{ave}$ represents the amplification of permanent axial strain caused by PSAR, the reciprocal
550 of $(R_s)_{ave}$ represents the decreasing rate of failure loading number. As a result, Eq. (26) is mod-
551 ified by adding the reciprocal of $(R_s)_{ave}$ to capture the effect of PSAR on pavement life against
552 rutting as shown in Eq. (29). It is noted that $(\sigma_a)_{max}$ and $(\tau_{a\theta})_{max}$ are stress states in laboratory
553 test through multi-ring shear apparatus, and they are equal to vertical stress, $(\sigma_z)_{max}$, and shear
554 stress, $(\tau_{yz})_{max}$, used in GAMES software.

$$555 N_{fS} = \beta_m \cdot \beta_{s1} \cdot \{1.365 \times 10^{-9} \cdot \varepsilon_a^{-4.477 \cdot \beta_{s2}}\} / \exp\left(\beta_{PSAR} \frac{(\tau_{yz})_{max}}{(\sigma_z)_{max}}\right) \quad (29)$$

556 To apply Eq. (29) into pavement life prediction, it is necessary to determining the suitable po-
557 sition in subgrade layer to estimate the $(\sigma_z)_{max}$ and $(\tau_{yz})_{max}$ through GAMES. To investigate how
558 $(\sigma_z)_{max}$ and $(\tau_{yz})_{max}$ change with depth, Section A and layer moduli in Aug are chosen to build a
559 model as shown in Fig. 21. As a consequence, Fig. 22 illustrates the σ_z and τ_{yz} in different depth,
560 z , and corresponding $(R_s)_{ave}$. It is obvious that σ_z and τ_{yz} show same tendency regardless of h . σ_z
561 reaches the largest value just below the wheel loading ($y=0$) and decreases with y . On the other

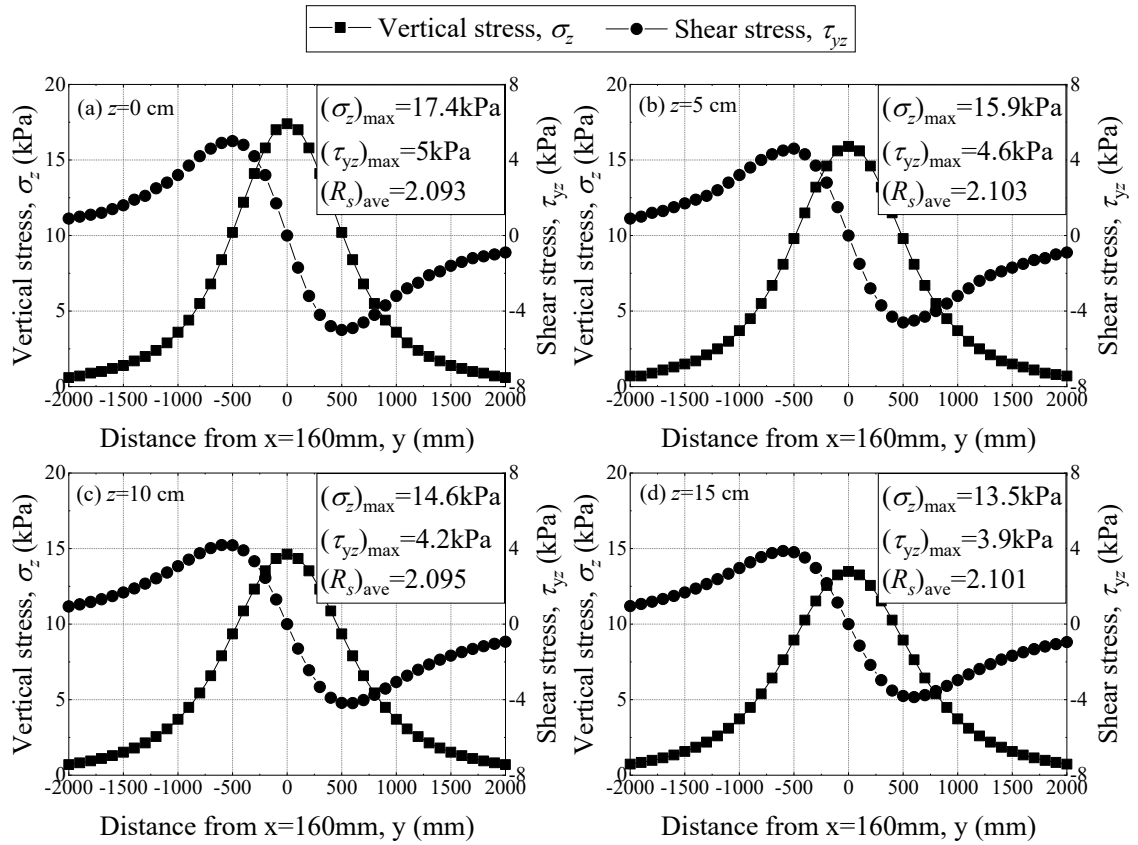
562 hands, τ_{yz} is zero just below the wheel loading and increases to the largest value at $y=600\text{mm}$
 563 then decreases. When the z increases, both $(\sigma_z)_{max}$ and $(\tau_{yz})_{max}$ decreases. $(R_s)_{ave}$ in all conditions
 564 are around 2.1. Consequently, it is suggested to set the h as 10cm, same depth in convergent
 565 analysis of E_3 as shown in Fig. 12.



566

567

Fig. 21 Stress states calculation point in subgrade layer.



568

569

Fig. 22 σ_z and τ_{yz} in different depth and corresponding $(R_s)_{ave}$.

570

Allowable loading number against rutting failure calculated through Eq. (29) in all eight sec-

571

tions are shown in Fig. 23. It is obvious that PSAR greatly decreases calculated pavement life

572

and N_{fs} with considering PSAR is most close to actual measured failure loading number. It is

573

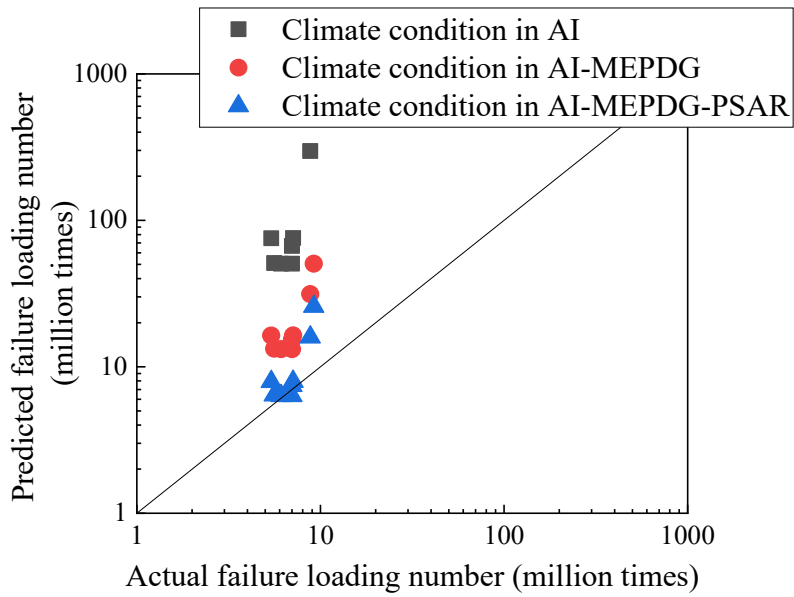
concluded the finally modified rutting model, AI-MEPDG-PSAR model, is useful and reliable

574

to predict the allowable loading number against rutting of flexible pavements especially for

575

roads located in cold regions like Hokkaido.



576

577

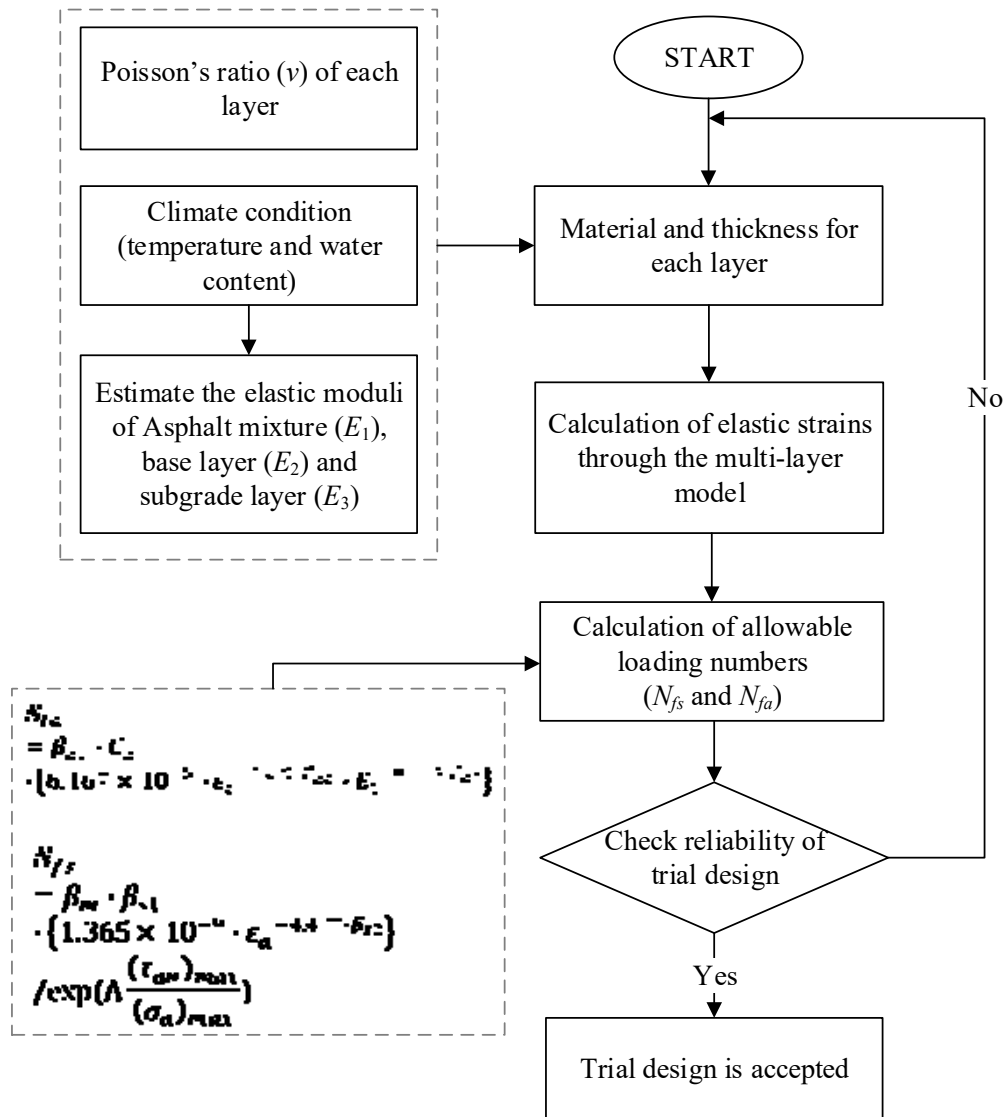
Fig. 23 Predicted N_{fs} considering PSAR.

578 Finally, the Fig. 24 illustrates the sequence in modified Japanese flexible pavement design

579 guide. It should be noted that the modification achieved in this study specially focused on the

580 base/subgrade layer mechanical properties and the rutting failure criterion as shown in the

581 comparison between Fig. 24 and Fig. 2.



582

583

Fig. 24 Sequence in modified Japanese flexible pavement design guide.

584 **5. Conclusions**

585 The following findings can be mainly obtained:

- 586 ● To modify current Japanese design guide by replacing constant subgrade layer moduli with
- 587 a variant relating to water content fluctuation and freeze-thaw history, newly proposed
- 588 modified Ng model, long-term measured in-situ base and subgrade layer water content,
- 589 and laboratory obtained SWCC are used. Calculated pavement life against rutting and fa-
- 590 tigue cracking proves that both water content fluctuation and freeze-thaw action degrade

591 stiffness of base and subgrade layer and finally decrease the pavement life of asphalt pave-
592 ments in cold regions.

593 ● Convergence calculation are essential since the rigidity changes with pavement structures
594 even if the influence of environmental conditions is taken into consideration. Environmen-
595 tal condition dependence has a greater effect on pavement life in pavement structures such
596 as high-standard roads, especially in the case of Japanese pavement where pavement life
597 against rutting is more of a problem than fatigue cracking.

598 ● Principal stress axis rotation greatly amplifies the permanent strain compared with triaxial
599 repeated loading test usually without such stress states. Ratio of axial strain, $(R_s)_{ave}$, is used
600 to quantitatively describe the amplified axial strain caused by principal stress axis rota-
601 tion and added into rutting failure criterion to help increasing prediction accuracy and ap-
602 plicability.

603 These findings indicate that a detailed understanding of the mechanical behavior of the base
604 and subgrade layer with complex water content fluctuation, freeze-thaw history, and stress
605 states is essential to develop a mathematical model for the mechanical response of the base and
606 subgrade layer in cold regions, and incorporate it into the theoretical design method for pave-
607 ment structures. Besides, a modification on the structure of failure prediction model by consid-
608 ering principal stress axis rotation is also important to improve the prediction accuracy and
609 applicability of mechanical-empirical design method for pavement in cold regions. Conver-
610 gence analysis is recommended for users of proposed modified design method according to its
611 effect on resilient modulus since the incorporation of all the improvements mentioned in this
612 study into a program for pavement design and lifetime prediction could overcome the

613 cumbersome calculations caused during the convergence analysis. Further and more compre-
614 hensive studies including more test on unbound granular materials with various water contents,
615 local calibration with more tests pavements are recommended to examine the validity, limita-
616 tion of application, and so forth as these findings are obtained through limited experimental
617 conditions and only examined with some local test pavement projects.

618 **Acknowledgements**

619 This research was supported in part by Grant-in-Aid for Scientific Research (B) (20360206),
620 (C) (15K06214), and (A) (16H02360) from Japan Society for the Promotion of Science (JSPS)
621 KA-KENHI. Support from China Scholarship Council is also highly acknowledged.

622 **References**

- 623 [1] AASHTO 2008. Mechanistic-Empirical Pavement Design Guide: A Manual of Practice,
624 Washington.
- 625 [2] Aldrich HP. Frost penetration below highway and air-field pavement. Highw Res Board
626 Bull 1956;135:124-49.
- 627 [3] Asphalt Institute 1982. Research and Development of Asphalt Institute's Thickness De-
628 sign Manual, 9th ed. Asphalt Institute, College Park Md.
- 629 [4] ASTM, 2011, Standard Practice for Classification of Soils for Engineering Purposes
630 (Unified Soil Classification System) (D2487-11)
- 631 [5] Berg RL, Bigl SR, Stark JA, Durell GD. Resilient modulus testing of materials from
632 Mn/Road: phase 1. 1996. <https://doi.org/10.21949/1404573>

- 633 [6] Brown SF. Soil mechanics in pavement engineering. *Géotechnique* 1996;46(3):383-426.
634 <https://doi.org/10.1680/geot.1996.46.3.383>
- 635 [7] Cary CE, Zapata CE. Resilient modulus for unsaturated unbound materials. *Road Mater*
636 *Pavement Des* 2011;12(3):615–38. <https://doi.org/10.1080/14680629.2011.9695263>
- 637 [8] Clayton CRI. Stiffness at small strain: research and practice. *Geotech* 2011;61:5-37.
638 <https://doi.org/10.1680/geot.2011.61.1.5>
- 639 [9] Cole DM, Irwin LH, Johnson TC. Effect of freezing and thawing on resilient modulus
640 of a granular soil exhibiting nonlinear behavior. *Transp Res Rec J Transp Res Board*
641 1981;809:19-26.
- 642 [10] Fredlund DG, Xing A. Equations for the soil-water characteristic curve. *Can Geotech J*
643 1994;31(4):521-532. <https://doi.org/10.1139/t94-061>
- 644 [11] Fredlund MD, Wilson GW, Fredlund DG. Use of the grain-size distribution for estima-
645 tion of the soil-water characteristic curve. *Can Geotech J* 2002;39(5):1103-1117.
646 <https://doi.org/10.1139/t02-049>
- 647 [12] Gräbe PJ, Clayton CR. Effects of principal stress rotation on permanent deformation in
648 rail track foundations. *J Geotech Geoenviron Eng* 2009;135(4):555-565.
649 [https://doi.org/10.1061/\(ASCE\)1090-0241\(2009\)135:4\(555\)](https://doi.org/10.1061/(ASCE)1090-0241(2009)135:4(555))
- 650 [13] Han Z, Vanapalli SK. State-of-the-art: Prediction of resilient modulus of unsaturated
651 subgrade soils. *Int J Geomech* 2016;16(4):04015104.
652 [https://doi.org/10.1061/\(ASCE\)GM.1943-5622.0000631](https://doi.org/10.1061/(ASCE)GM.1943-5622.0000631)
- 653 [14] Huang YH, 2004. *Pavement Analysis and Design*, 2nd ed. Pearson Education, Inc.
- 654 [15] Inam A, Ishikawa T, Miura S. Effect of principal stress axis rotation on cyclic plastic

- 655 deformation characteristics of unsaturated base course material. *Soils Found*
656 2012;52(3):465-480. <https://doi.org/10.1016/j.sandf.2012.05.006>
- 657 [16] Ishikawa T, Sekine E, Miura S. Cyclic deformation of granular material subjected to
658 moving-wheel loads. *Can Geotech J* 2011;48(5):691-703. [https://doi.org/10.1139/t10-](https://doi.org/10.1139/t10-099)
659 099
- 660 [17] Ishikawa T, Lin T, Kawabata S, Kameyama S, Tokoro T. Effect evaluation of freeze-
661 thaw on resilient modulus of unsaturated granular base course material in pavement.
662 *Transp Geotech* 2019a;21:100284. <https://doi.org/10.1016/j.trgeo.2019.100284>
- 663 [18] Ishikawa T, Lin T, Yang J, Tokoro T, Tutumluer E. Application of the UIUC model for
664 predicting ballast settlement to unsaturated ballasts under moving wheel loads. *Transp*
665 *Geotech* 2019b;18:149-162. <https://doi.org/10.1016/j.trgeo.2018.12.003>
- 666 [19] Japan Meteorological Agency, Automated Meteorological Data Acquisition System.
667 <https://www.jma.go.jp/jp/amedas/>
- 668 [20] Japan Society of Civil Engineers, 2015. Characteristics and Evaluation of Subgrade and
669 Base Course Materials, Japan Society of Civil Engineers, Tokyo. [in Japanese]
- 670 [21] Japan Road Association, 2006. Pavement design manual, Japan Road Association, To-
671 kyo. [in Japanese]
- 672 [22] Johnson TC, Cole DM, Chamberlain EJ. Influence of freezing and thawing on the resili-
673 ent properties of a silt soil beneath an asphalt concrete pavement. U.S. Cold Regions
674 Research and Engineering Laboratory, CRREL Report 78-23. 1978. [http://hdl.han-](http://hdl.handle.net/11681/9380)
675 [dle.net/11681/9380](http://hdl.handle.net/11681/9380)
- 676 [23] Liang RY, Rabab'ah S, Khasawneh M. Predicting moisture-dependent resilient modulus

677 of cohesive soils using soil suction concept. J Transp Eng 2008;134(1):34-40.
678 [https://doi.org/10.1061/\(ASCE\)0733-947X\(2008\)134:1\(34\)](https://doi.org/10.1061/(ASCE)0733-947X(2008)134:1(34))

679 [24] Lin T, Ishikawa T, Yang J, Tokoro T. Evaluation of climate effect on resilient modulus
680 of granular subgrade material, Cold Reg Sci Technol 2020. (under review)

681 [25] Lin T, Ishikawa T, Luo B. Applicability of modified University of Illinois at Urbana–
682 Champaign model for unbound aggregate material with different water content, Transp
683 Res Rec 2019a;2673(3):439-449. <https://doi.org/10.1177/0361198119827530>

684 [26] Lin T, Ishikawa T, Tokoro T. Testing method for resilient properties of unsaturated un-
685 bound granular materials subjected to freeze-thaw action. Japanese Geotech Soc Spec
686 Publ 2019b;7(2):576-581. <https://doi.org/10.3208/jgssp.v07.089>

687 [27] Maina JW, Matsui K. Developing software for elastic analysis of pavement structure re-
688 sponses to vertical and horizontal surface loadings. Transp Res Rec J Transp Res Board
689 2004;1896(1):107-118. <https://doi.org/10.3141/1896-11>

690 [28] Maruyama K, Tako J, Kasahara A. Long-term performance of asphalt pavements at bibi
691 new test road. J JSCE E 2006;62(3):519-530. [in Japanese]
692 <https://doi.org/10.2208/jsceje.62.519>

693 [29] Maruyama K, Tako J, Kasahara A. Fatigue failure life prediction method of asphalt
694 pavement. J JSCE E 2008;64(3):416-426. [in Japanese]
695 <https://doi.org/10.2208/jsceje.64.416>

696 [30] Miura K, Miura S, Toki S. Deformation behavior of anisotropic dense sand under prin-
697 cipal stress axis rotation. J Soils Found 1986;26(1):36-52.
698 <https://doi.org/10.3208/sandf1972.26.36>

- 699 [31] Mori T, Kamiya K, Chiba T, Uzuoka R, Kazama M. The functional model of the soil-
700 water characteristic curve used the logistic function during cyclic shearing. 44th Japan
701 national conference on geotechnical engineering, Proc dom conf. 2009. p.1519-20. in
702 Japanese.
- 703 [32] NCHRP 2004. Guide for mechanistic-empirical design of new and rehabilitated pave-
704 ment structures.
- 705 [33] Ng CWW, Zhou C, Yuan Q, Xu J. Resilient modulus of unsaturated subgrade soil: ex-
706 perimental and theoretical investigations. *Can Geotech J* 2013;50(2):223-232.
707 <https://doi.org/10.1139/cgj-2012-0052>
- 708 [34] Seed HB, CHAN CK, Monismith CL. Effects of repeated loading on the strength and
709 deformation of compacted clay. *Highw Res Board Proc* 1955;34:541-558.
- 710 [35] Simonsen E, Janoo VC, Isacsson U. Resilient properties of unbound road materials dur-
711 ing seasonal frost conditions. *J Cold Reg Eng* 2002;16(1):28–50.
712 [https://doi.org/10.1061/\(ASCE\)0887-381X\(2002\)16:1\(28\)](https://doi.org/10.1061/(ASCE)0887-381X(2002)16:1(28))
- 713 [36] Simonsen E, Isacsson U. Soil behavior during freezing and thawing using variable and
714 constant confining pressure triaxial tests. *Can Geotech J* 2001;38(4):863-875.
715 <https://doi.org/10.1139/t01-007>